UNIVERSITY OF OKLAHOMA

GRADUATE COLLEGE

SOLAR-DRIVEN DIRECT BLUE 71 DYE DECONTAMINATION WITH METAL- AND NON-METAL-DOPED TITANIUM DIOXIDE PHOTOCATALYST

A THESIS

SUBMITTED TO THE GRADUATE FACULTY

in partial fulfillment of the requirements for the

Degree of

MASTER OF SCIENCE

IN CHEMICAL ENGINEERING

By HOANG THAO VY NGUYEN

Norman, Oklahoma

2025

SOLAR-DRIVEN DIRECT BLUE 71 DYE DECONTAMINATION WITH METAL- AND NON-METAL-DOPED TITANIUM DIOXIDE PHOTOCATALYST

A THESIS APPROVED FOR THE
SCHOOL OF SUSTAINABLE CHEMICAL, BIOLOGICAL AND MATERIALS ENGINEERING

BY THE COMMITTEE CONSISTING OF

Dr. Ngoc Bui, Chair

Dr. Lance Lobban

Dr. Bin Wang

ACKNOWLEDGEMENT

First and foremost, I would like to convey my deepest gratitude to Dr. Ngoc Bui for providing me with an opportunity to be under her supervision. Despite hailing from a different educational background, she placed her trust in me and provided constant feedback and sound advice throughout the duration of my program. Her counsel has pushed me towards the completion of this thesis and my degree. I also could not have undertaken this journey without my defense committee, Dr. Lance Lobban and Dr. Bin Wang, who generously provided knowledge and expertise.

I would like to express my sincere gratitude to Dr. Galizia, who provided me with access to the UV-Vis spectrometer. I am grateful to Dr. Saparov at the Department of Chemistry and Biochemistry for his permission to characterize my samples with the UV-vis-near-infrared spectrometer and spectrofluorometer. I am also thankful to Dr. Madden and Dr. Larson at the Samuel Roberts Noble Microscopy Laboratory for their training and access to the SEM-EDX and XRD instruments.

I extremely appreciate Dr. Daniel Resasco for his engaging lectures that equipped me with valuable insights and fundamentals. I am indebted to Dr. Thanh-Dong Pham and Dr. Hanh T. Nguyen at the VNU University of Science, who familiarized me with scientific research and critical thinking skills.

I am also grateful to Dr. Van Le for showing me how to conduct SEM, UV-Vis, and CV techniques, as well as teaching essential lab skills when I first started in the lab. I would like to express my sincere appreciation to Lucas Condes for his enthusiastic assistance in training me in various testing methods. Special thanks to Dilruba Popy for her supportive instruction in conducting the UV-Vis DRS and PL measurements, as well as in analyzing the corresponding data. Thanks should also go to Minh Tran, who assisted me with the zeta potential measurement. I extend my sincere thanks to Phuong Nguyen, Thy Ho, Eymi Layza Escobar, Ranuja Bandara, Ngan Thai, and Nam Do for their openness in sharing and discussing scientific perspectives with me. Many thanks to all my colleagues in the Bui Lab for sharing their time to support me.

I would also like to express my heartfelt thanks to my grandmothers, who always encouraged me, and to my parents and brother, who supported me with their best efforts. Last but not least, I would like to sincerely thank all my dearest friends for dedicating their precious time to supporting me and sharing in my happiness and sadness.

TABLE OF CONTENTS

LIST OF ABBREVIATIONS

a.u.	Arbitrary unit
CB	Conduction band
C_0	Initial concentration of Direct Blue 71 in the solution
C_f	Final concentration of Direct Blue 71 in the solution
C_t	Concentration of Direct Blue 71 in the solution at a specific time interval t
DB71	Direct Blue 71
DI water	Deionized water
E_g	Band gap energy
EDX	Energy-dispersive X-ray spectroscopy
L-AA	L-Ascorbic acid
MO	Methyl orange
OV	Oxygen vacancy
pH_{zpc}	pH value at the point of zero charge
PL	Photoluminescence
SEM	Scanning electron microscope
UV-Vis	Ultraviolet-visible
UV-Vis DRS	Ultraviolet-visible diffuse reflectance spectroscopy
RB	Rose Bengal
VB	Valence band
XRD	X-ray powder diffraction

LIST OF FIGURES

Figure 4.12. DB71 removal performance of Fe,N-TiO_2 with respect to time (a), and determination of the kinetic constant of DB71 photodegradation by Fe,N-TiO_2. [m_{cat} = 0.2 g/L, C_{0_DB71} = 20 ppm, pH = ~7].

LIST OF TABLES

ABSTRACT

The presence of azo dyes in aqueous environments poses numerous environmental threats that require effective and sustainable decontamination methods. Herein, commercial TiO_2 photocatalysts were co-doped with N and one metal dopant (including Al, Zn, Cr, Fe, Ni, or Cu) for the advanced degradation of Direct Blue 71 (DB71), a typical representative of azo dye, under simulated solar conditions. Nitrogen is hypothesized to trap photogenerated holes, while the metal dopant may serve as a sink for excited electrons. All co-doped TiO_2 samples exhibited an improvement in DB71 adsorption capability compared to pristine TiO2 owing to the increased surface area. Meanwhile, their photocatalytic performances were promoted in different manners, highlighting the importance of the dopant content and the alignment between the impurity energy level and the band structure of TiO2. Among synthesized samples, Fe/N-doped TiO2 displayed the superior photodegradation efficiency of DB71, with approximately 93% of dye being removed in 2 h, due to its highest visible-light absorption capacity and suppressed recombination rate of electron-hole pairs. The DB71 photodegradation of Fe,N-TiO_2 sample was primarily attributed to the photogenerated holes, followed by singlet oxygen radicals. Photogenerated holes and singlet oxygen radicals played pivotal roles in degrading DB71 by Fe,N-TiO_2 under solar-irradiated conditions. The optimal photocatalytic removal of DB71 of Fe,N-TiO_2 occurred at neutral pH, highlighting the unnecessary chemical additions for pH adjustment in actual wastewater systems.

Keywords: Co-doped TiO2; DB71 photocatalytic degradation; visible-light excitation.

1. INTRODUCTION

The extensive use of freshwater for dyeing and finishing textile products places considerable strain on water resources and environmental concerns. Among the dye residues that contaminate the environment, azo dyes with a poorly biodegradable nature are discharged in large amounts directly into water bodies, primarily due to the inefficient textile dyeing process. This poses dire ecotoxicological threats and harmful effects on living creatures. [1, 2] Despite the low acute toxicity of azo dyes, this chemical class and its decomposed products, particularly aromatic amines, tend to induce high levels of mutagenicity and carcinogenicity chronically. [1-4] Thus, addressing wastewater treatment with dye residues, especially those of azo dyes, is a pressing concern that requires immediate attention.

Various techniques have been employed to decontaminate azo dyes from the environment, including adsorption, coagulation, flocculation, membrane filtration, biological methods, and photocatalysis. Adsorption and membrane filtration processes are unable to degrade pollutants, as they can only be transferred from the liquid to the solid interface. Coagulation-flocculation and biological treatment approaches raise concerns about harmful secondary sludge. Meanwhile, advanced oxidation process using photocatalysts is an attractive, destructive approach to treat polluted organic dye compounds, with preeminence. Of note, photocatalysis can occur under mild operating conditions and utilize solar energy as an excitation source, rapidly degrading and mineralizing pollutants with minimal chemical use through in-situ radical formation. [1, 5, 6]

Metal oxides (TiO_2, ZnO, In_2O_3, Co_3O_4, etc.), metal sulfides (CdS, MoS_2, ZnS, etc.), ternary compounds (perovskites, tungstate, titanates), and non-metal semiconductors (g-C_3N_4, graphene oxide, covalent organic framework, etc.) have been successfully synthesized and applied for dye photodegradation in aqueous environments. [7-17] TiO_2 is among the most commonly utilized photocatalytic materials, especially for the degradation of organic pollutants, by virtue of its affordability, abundance, non-toxicity, strong oxidizing capability of photoinduced holes, and resistance to corrosion and chemical degradation. [18, 19] However, the large-scale application of the commercially available TiO_2 products is curbed by its wide band gap (~3.2 eV), which necessitates the stimulation of ultraviolet light, as well as the rapid recombination rate of photogenerated electrons and holes. [20] Hence, modification of pure TiO_2 material toward the improvement in its visible light photoactivity is needful.

Doping with impurities is one of the potential strategies to effectively conquer the drawbacks of TiO_2 to improve its photocatalytic performance. [18, 21, 22] Indeed, the band gap of TiO_2 is expected to be narrowed, possibly because of either the electronic coupling effect between doping ions and TiO_2 or the introduction of discrete energy states within the band gap (i.e., beyond the VB or beneath the CB of TiO_2), thereby enhancing the visible light absorption capacity. A variety of dopants have been studied, including nonmetals (C, N, F, S, etc.), transition metals (Fe, Cu, Mo, Ru, Co, V, etc.), noble metals (Au, Ag, Pt, etc.), and rare earth metals (La, Er, Y, Eu, etc.). [18, 21-23] Of which, non-metal dopants have captured great attention since they constrict the band gap of TiO_2 through introducing new electronic states between the valence and conduction bands, thus extending the visible light harvesting capacity. [24] Specifically, nitrogen, with its stability and low ionization energy, is considered a promising dopant for effectively red-shifting the absorption edge of TiO_2 by the hybridization between doped N *2p* orbitals and O *2p* orbitals. [9, 25] Nevertheless, TiO_2 photocatalysts doped with non-metal elements still exhibit a high recombination rate of photogenerated charge carriers. [9, 26] Co-doping TiO_2 with N and another dopant, such as metals, is expected to prevent the quick recombination of these photo-induced charges, inducing the synergistic effects of superiorly enhancing optical efficiency and boosting photocatalytic activity compared to TiO_2 modified with single components. [22, 27] In essence, the non-metal dopant is expected to trap excited holes, while the metal dopant may operate as a sink for photogenerated electrons. [27-29] Metal dopants with varying electronic structures would exert different effects on the photocatalytic behaviors of TiO_2. Thus, this study focused on investigating the photocatalytic activity of commercial TiO_2 co-doped with N and one metallic dopant (i.e., Al, Zn, Cr, Fe, Ni, or Cu) under simulated solar conditions for the degradation of azo dyes in the aqueous environment. DB71, which finds wide applications in the textile, paper, and plastic industries [30], is representative of azo dyes in its class; therefore, we chose it as a model for the photocatalytic degradation process. Besides, the concentration of DB71 can be simply calculated using UV–Vis spectroscopy at its maximum absorbance wavelength of λ = 586 nm.

2. BACKGROUND

2.1. Overview of dye pollution

2.1.1. Dye definition, composition, and classification

Dyes are substances that lend color to various materials, including textiles, plastics, paper, cosmetics, and so on. Dyes are generally organic compounds comprising two primary components: chromophore and auxochrome. Chromophore is a covalently bonded chemical group, such as –N=O, –C=O, –C=N, –C≡N, and –N=N–, accounting for the dye color owing to its ability to absorb specific wavelengths in the visible light region, while an auxochrome acts as a color-modifying functional group attached to the chromophore structure (e.g., –OH, $–NH_2$, –COOH, –Cl, etc.). [31] Dyes can be classified into natural and synthetic categories based on their origin. The latter is subdivided into other groups, as partly shown in **Table 2.1**.

Table 2.1. Classification of synthetic dyes. [1, 31, 32]

Dye type	Properties
Acid dye	o Contain sulphonic acid ($-SO_3H$) and carboxylic acid (-COOH) groups o Anionic, water-soluble dyes o Neutral to acidic dye solutions are used to color the fiber from these dyes
Basic dye	o Contain amino or dialkylamino groups o Cationic, water-soluble dyes
Direct or substantive dye	o Water-soluble compounds o Offer good brightness and intense color o Can be applied directly to the fiber
Disperse dye	o Water-insoluble compounds o Applied to the fabric in a dispersed form with the aid of stabilizing agents like phenol, cresol, or benzoic acid.
Reactive dye	o Most permanent dyes, creating long-lasting colors o Contain a reactive group that directly reacts with the hydroxyl or amino groups of the fiber.

Mordant dye	o They do not bind directly but require a mordant (i.e., binding agent) to dye the fiber; different mordants bring about varying final fiber colors o Most of the natural dyes are mordant dyes
Vat dye	o Insoluble in water and incapable of dyeing fabrics directly o Solubilize when being reduced via alkaline solutions and transform to insoluble dye after consecutive oxidation

Besides that, dyes are also classified based on the functional group that determines their color – azo dyes, nitro dyes, nitroso dyes, triphenylmethane dyes, quinone-imine dyes, and indophenol dyes, to name a few. Notably, azo dyes, characterized by azo groups (–N=N–), constitute the highest portion of dye production and represent about 70% of all dyes used in industry as well, mostly in textiles, food, printing, and paper manufacturing. [1, 4, 31]

2.1.2. Dye pollution and corresponding environmental risks

Over 7×10^5 metric tons of synthetic dyes are produced each year worldwide, with the textile industry being the most significant consumer, accounting for over 10^4 metric tons. [1, 32, 33] However, the extensive use of freshwater for dyeing and finishing textile products places considerable strain on water resources and environmental concerns. [32, 34] Moreover, the large volumes of effluent-containing dye residues discharged during these processes account for roughly 20% of industrial water pollution worldwide and make the textile industry the second largest contributor to polluting clean water bodies (following agricultural activities). [32, 35] According to the literature, outflow dye concentrations vary from 10 to 7000 mg/L, depending upon the dye categories and application fields, with more typical values being below 1000 mg/L. [36, 37]

Dye suspension in wastewater appears as light-scattering particles, thus increasing turbidity. This blocks sunlight penetration, which disrupts the photosynthesis of aquatic organisms and the self-purification of water due to reduced dissolved oxygen. [32, 38] Among the dye residues that contaminate the environment, azo dyes with a poorly biodegradable nature are discharged in large amounts directly into water bodies, mainly due to the inefficient textile dyeing process. This poses dire ecotoxicological threats and harmful effects on living creatures. [1, 2] Despite the low acute toxicity of azo dyes, this chemical class and its decomposed products, particularly aromatic amines, tend to induce high levels of mutagenicity and

carcinogenicity chronically. [1-4] Therefore, addressing wastewater treatment with dye residues, especially those of azo dyes, is an urgent issue that requires immediate attention.

2.1.3. Treatment methods of dye residues in aqueous media

Various techniques have been investigated to decontaminate dye residues from the environment. Adsorption has been commonly used for the removal of a diverse range of target contaminants. It is technically straightforward and highly effective, with fast kinetics, yet a non-selective and non-destructive process in which pollutants can only be transferred from the liquid to the solid phase. In addition, coagulation and flocculation are potent methods for removing various organic compounds and suspended particles; however, the resultant harmful secondary sludge requires further treatment. Biological treatment methods, despite their affordability and eco-friendliness, also encounter similar challenges besides sluggish transformation kinetics. Meanwhile, membrane filtration has great potential to separate pollutants, even at high concentration, from the aqueous environment with low generation of solid waste. Despite that, this method is limited by high investment and operational costs, high energy demand, and low throughput. Currently, advanced oxidation process using photocatalysts is an attractive, destructive approach to treat polluted organic dye compounds, with preeminence. Notably, photocatalysis can occur under mild operating conditions and utilize solar energy as an excitation source, rapidly degrading and mineralizing pollutants with minimal chemical use through in-situ radical formation. [1, 5, 6] The merits and demerits of treatment methods of dye residues in aqueous media are summarized in **Table 2.2**.

Table 2.2. Merits and demerits of dye treatment methods. [1, 5, 6]

Method	Main characteristics	Merits	Demerits	Ref.
Adsorption	Adsorbed molecules, ions, or particles are attracted to a solid adsorbent surface.	▪ Technologically simple ▪ Wide variety of target contaminants ▪ Effective process with fast kinetics	▪ Nondestructive ▪ Non-selective ▪ Rapid saturation and clogging of the adsorbent	[39-42]

Coagulation and flocculation	These two processes are often employed together. Coagulation is the initial step that involves the addition of chemicals to neutralize particle charges and destabilize the particle colloids. Flocculation follows coagulation and is used to promote the growth of larger flocs for easier removal from water.	Effective process in removing various organic compounds as well as suspended particles	▪ High operational costs ▪ Generate harmful sludge that needs further treatment	[43-45]
Membrane filtration	Membrane filtration separates particles in liquid solutions or gas mixtures according to their size charge. It employs a semi-permeable membrane to eliminate unwanted contaminants and particles.	▪ Minimal space needed ▪ No chemicals are needed ▪ Simple, rapid, and efficient, even at high concentrations ▪ Low solid waste generation	▪ High investment costs, particularly for small and medium-sized industries ▪ High maintenance and operation costs ▪ High energy demand ▪ Nondestructive ▪ Low throughput ▪ Membrane fouling	[46-48]
Biological methods	Microorganisms are employed to degrade organic pollutants	▪ More easily applicable ▪ Require fewer chemical reagents	▪ Sluggish process ▪ Need to create favorable conditions	[49-51]

		▪ Less expensive ▪ Energy-saving ▪ Environmentally safe	▪ Incorruptible with persistent substances (e.g., azo dyes) ▪ Generation of biological sludge and uncontrolled degradation products	
Photo-catalysis	Photocatalysis employs semiconductor photocatalysts and light as energy sources to break down organic pollutants.	▪ In-situ production of reactive radicals ▪ Rapid degradation with minimal use of chemicals. ▪ Efficient for persistent molecules ▪ No production of sludge ▪ Ability to mineralize pollutants ▪ Only mild temperature and pressure conditions are required.	▪ Formation of byproducts ▪ Limited applicability at an industrial scale ▪ Not economically viable for small and medium-sized industries	[17, 52, 53]

2.2. Overview of photocatalysis

2.2.1. Definition of photocatalysis

Photocatalysis, or a photocatalytic reaction, refers to a chemical reaction stimulated by the light absorption of a photocatalyst that remains unchanged during the reaction. [54, 55] Basically, photocatalytic reactions are classified into two types: homogeneous and heterogeneous processes. Homogeneous photocatalysis occurs when the catalyst is in the same phase as the reactant(s), while heterogeneous photocatalysis occurs when the catalyst and reactant(s) are in different phases. [56, 57] Particularly, heterogeneous photocatalysis has gained significant attention due to its potential for environmental remediation, water purification, energy applications, organic synthesis, and health self-sterilization. [56, 58]

2.2.2. Mechanism of photocatalysis

a. Band energy structure:

Photocatalysts are fundamentally semiconductor materials that consist of:

- Valence band (VB), a continuous band of energy where orbitals are filled with electrons. This is the region where the electron is strongly bonded to the atom, inflexible, and has the lowest energy on the energy scale.

- Conduction band (CB), the region with the highest energy level where orbitals are not filled with electrons. When the semiconductor is excited, the valence electrons can move up to the conduction band and reside there, and the electrons in the conduction band behave like free electrons.

- The zone between the valence and conduction bands is referred to as the forbidden region (**Figure 2.1**), where no electrons can occupy due to the nonexistence of orbitals. The width of the forbidden region is called the band gap, representing the minimum energy necessitated to excite an electron from the valence band to the conduction band. [56, 57]

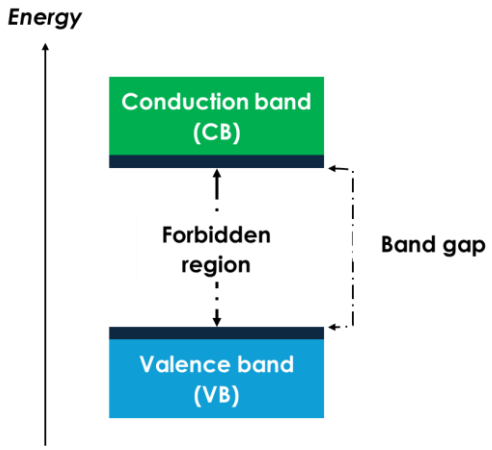

Figure 2.1. Energy band structure of a semiconductor.

b. Mechanism of contaminant photodegradation:

The heterogeneous photocatalytic process includes six stages (**Figure 2.2**), which can be divided into four primary processes: light absorption (stage 1), charge stimulation (stage 2), charge separation and transfer (stages 3 and 4), and surface electrocatalytic reactions (stages 5 and 6). [59]

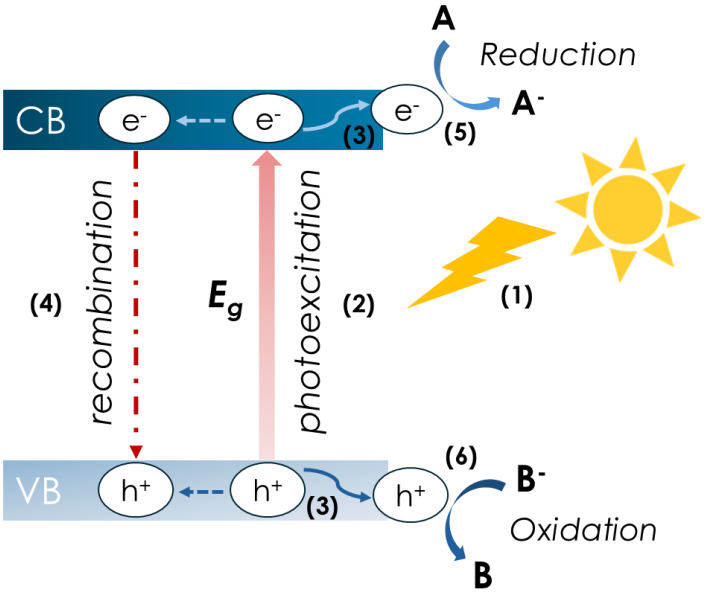

Figure 2.2. Mechanism of the heterogeneous photocatalysis process. [56, 57, 59]

The light-harvesting capacity of a photocatalyst is known to be strongly dependent on its surface morphology and structure. When the semiconductor is excited by light photons with energy greater than or equal to its band gap energy (E_g), electrons in the VB can absorb energy and jump onto the conduction band, leaving corresponding positively charged holes (h^+) in the VB (stage 2).

$$\text{Photocatalyst} + h\nu \rightarrow e^-_{CB} + h^+_{VB} \quad (2.1)$$

Since the difference between the potentials of the VB and the CB is relatively large, if electrons and holes do not react with other substances immediately or are not stored by an intermediate, they will quickly recombine in bulk and/or on the surface (stage 4) and then release energy in the form of heat or light. Only sufficient energetic electrons and holes that migrate to the semiconductor surface without recombination can be trapped by the surface-active sites and further stimulate the electro-catalytic reduction (stage 5) and oxidation (stage 6) reactions of the reactants adsorbed on the semiconductor, respectively. As a result, free radicals ($^{\bullet}OH$, $^{\bullet}O_2^-$, etc.) are formed and continue to decompose, and ideally mineralize pollutants into CO_2 and H_2O. It should be noted that the possibility of surface reactions occurring when the reduction and oxidation potentials are more positive and negative, respectively, than the CB and VB levels.

$$e^- + O_2 \rightarrow {}^{\bullet}O_2^- \quad (2.2)$$

$$2\ {}^{\bullet}O_2^- + 2\ H_2O \rightarrow H_2O_2 + 2\ HO^- + O_2 \quad (2.3)$$

$$^{\bullet}O_2^- + h^+ \rightarrow {}^1O_2 \quad (2.4)$$

$$e^- + H_2O_2 \rightarrow {}^{\bullet}OH + HO^- \quad (2.5)$$

$$h^+ + H_2O \rightarrow {}^{\bullet}OH + H^+ \quad (2.6)$$

$$h^+ + HO^- \rightarrow {}^{\bullet}OH \quad (2.7)$$

$$(^{\bullet}OH, {}^1O_2, h^+, e^-\ldots) + \text{Pollutant} \rightarrow CO_2 + H_2O \quad (2.8)$$

Basically, effective photodegradation of contaminants requires light sources with sufficient energy, a long charge carrier lifetime (i.e., low recombination rate), and proper redox potentials. Besides, it is also governed by operating conditions, including pH, temperature, photocatalyst content, light intensity, and others.

2.2.3. Photocatalysts employed for dye degradation in the water environment

Table 2.3 lists some examples of the most studied and innovative semiconductor materials, whether in standalone or composite forms, for photocatalytic wastewater. purification.

Table 2.3. Common and novel photocatalysts employed for dye degradation in the water environment.

Photocatalyst type	Examples	References
Metal oxides	TiO_2, ZnO, WO_3, CeO_2, In_2O_3, Co_3O_4	[53, 60-63]
Metal sulfides	CdS, MoS_2, ZnS, CuS, Bi_2S_3	[10, 12, 64]
Ternary compounds	Perovskites [ABX_3] ($NdFeO_3$, $SrZnO_3$) Tungstate ($CuWO_4$, Bi_2WO_6) Titanates ($BaTiO_3$, $La_2Ti_2O_7$)	[13, 65] [11, 15] [8, 14]
Non-metal semiconductors	g-C_3N_4, graphene oxide, covalent organic framework, carbon quantum dots	[7, 16, 66, 67]

Metal oxides, metal sulfides, ternary compounds as well as non-metal semiconductors have been successfully synthesized and applied for dye photodegradation in aqueous environments. [11, 13, 14, 41, 42, 61, 62, 64, 65, 68] Saleh synthesized ZnO nanospheres with hierarchical structures through the ethylene glycol solvent hydrothermal method for the

photodegradation of methyl orange (MO) in aqueous medium. [69] The resultant material displayed efficient MO degradation without observable disturbance from the co-existing anions (i.e., CO_3^{2-}, HCO_3^-, SO_4^{2-}, and NO_3^-) and cations (K^+, Na^+, Ca^{2+}, Sr^{2+}, and Ba^{2+}); however, with the need for UV light excitation. Meanwhile, solvent-exfoliated Bi_2S_3 nanosheets could decompose roughly 77% of MO in 4 h under visible light irradiation. The relatively slow degradation kinetics might be due to the low redox potentials induced by its narrow band gap of ~1.1 eV. [12] Kumar et al. developed $CuWO_4$ nanoparticles through a combustion method, utilizing *Butea monosperma* leaves as an alternative reducing and capping agent. This approach presents a promising photocatalyst with enhanced light absorption for degrading rose Bengal (RB) dye under visible light irradiation. Indeed, the degradation efficiency of RB by the synthesized $CuWO_4$ sample was beyond 96% in 150 min and decreased by only 7% after four testing cycles. [15] Besides, Sainin et al. presented the outstanding sunlight-promoted decomposition of a mixture of MO and metanil yellow dyes by carbon dots modified with nitrogen-sulfur-phosphorus. Notably, this material was easily obtained by microwaving a mixture of polyethylene glycol (as a C matrix), phosphoric acid, and L-cysteine (as P, N, and S impurity sources), resulting in surface defects that significantly extend the light-harvesting capability. [70]

2.3. Overview of TiO_2

2.3.1. TiO_2 crystalline phases

In nature, TiO_2 occurs in three polymorphs: anatase, rutile, and brookite (**Figure 2.3**). Brookite is seldom reported as a photocatalyst due to synthesis challenges. [71] Rutile is a thermodynamically stable phase, while the anatase phase is metastable. The experimental band gap of rutile is lower than that of anatase (i.e., ~3.0 eV vs. ~3.2 eV), thereby exhibiting better visible-light response. [19, 71, 72] Meanwhile, anatase is typical of higher photocatalytic activity owing to its finer grain size (i.e., higher surface area), slower recombination rate of photoactivated charge carriers, and higher electron mobility. [19, 73] In addition, anatase dominates the low-temperature form of pure titania, found within the range of 300–550 °C, and it gradually transforms into rutile when heated. [73]

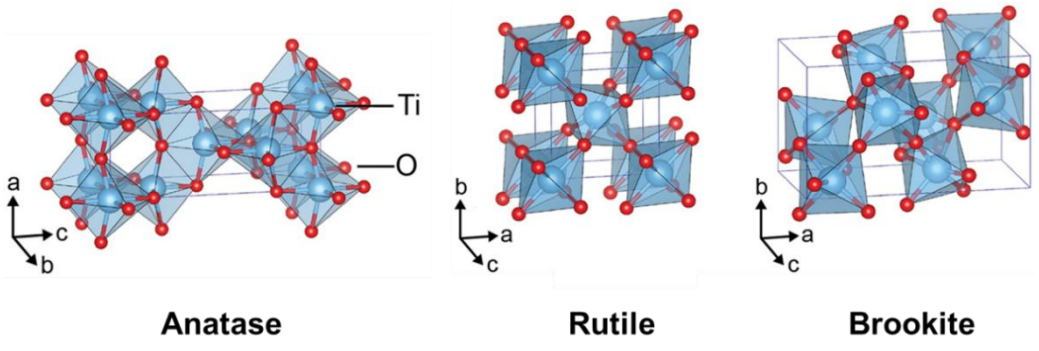

Figure 2.3. Crystalline phases of TiO_2. [74]

It is uncommon to obtain sole polymorphs as TiO_2 syntheses usually yield various mixtures of anatase and rutile. TiO_2 photocatalysts with mixed anatase/rutile phases also perform higher photocatalytic activity than single-phase titania due to synergistic effects that promote spatial separation of charge carriers, broaden the light absorption range, and diversify redox potential. [73, 75] In addition to the surface area, the proportions of anatase and rutile in TiO_2 have a significant influence on its photocatalytic activity. [76, 77]

2.3.2. Advantages and disadvantages of TiO_2 photocatalyst

TiO_2 is among the most widely utilized photocatalysts, especially for environmental applications, by virtue of its affordability, abundance, non-toxicity, strong oxidizing capability of photoinduced holes, and resistance to corrosion and chemical degradation. [18, 19] Nonetheless, the wide band gap (~3.2 eV) of the commercially available TiO_2 products necessitates excitation from a light source with a wavelength $\lambda \leq 385$ nm, limiting the utilization of sunlight as less than 5% of the solar spectrum falls within the UV range (**Figure 2.4**). [20] Furthermore, the photocatalytic activity of TiO_2 is negatively impacted by the rapid recombination rate of photogenerated electrons and holes. [18, 63] Hence, modifying pure TiO_2 material to narrow its band gap and promote the charge carrier separation to improve its photocatalytic performance is needed.

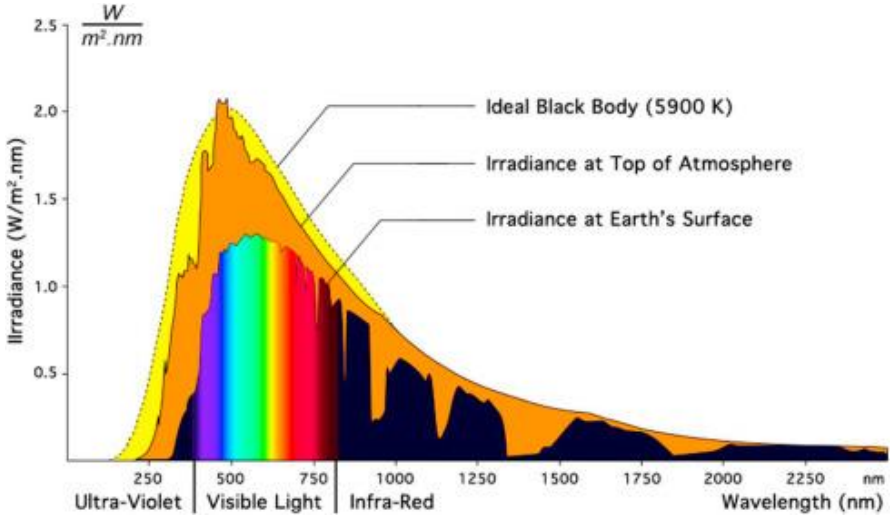

Figure 2.4. Spectrum of solar irradiation. [20]

2.3.3. TiO_2 doping strategies

Doping with impurities has been widely employed to conquer these drawbacks of TiO_2 toward the improvement in its visible light photoactivity. [18, 21, 22] Indeed, the band gap of TiO_2 is expected to be narrowed, possibly because of either the electronic coupling effect between doping ions and TiO_2 or the introduction of discrete energy states within the band gap (i.e., beyond the VB or beneath the CB of TiO_2), thereby enhancing the visible light absorption capacity. Besides, the impurity energy levels created by an adequate dopant dose can serve as a trapping center for photogenerated electrons to efficiently separate the photogenerated hole-electron pairs, deferring their recombination. [22, 23]

Of which, non-metal dopants have captured great attention since they constrict the band gap of TiO_2 through introducing new electronic states between the valence and conduction bands, thus extending the visible light harvesting capacity. [24] Specifically, nitrogen, with its stability and low ionization energy, is considered a promising dopant for effectively red-shifting the absorption edge of TiO_2 by the hybridization between doped N *2p* orbitals and O *2p* orbitals. [9, 25] Nevertheless, TiO_2 photocatalysts doped with non-metal elements still exhibit a high recombination rate of photogenerated charge carriers. [9, 26] Co-doping TiO_2 with N and another dopant, such as metals, is expected to prevent the quick recombination of these photo-induced charges, inducing the synergistic effects of superiorly enhancing optical efficiency and boosting photocatalytic activity compared to TiO_2 modified with single components. [22, 27] In essence, the non-metal dopant is expected to trap photogenerated holes, while the metal dopant may operate as a sink for excited electrons. [27-29] Noticeably, the photoreactivity of TiO_2 co-doped with metals and nonmetals complicatedly depends on

several dopant-related factors, including their amount, energy level and distribution within the TiO_2 lattice, electronic configuration of the outer shell, and so on. [22, 78] Thus, this study focused on investigating the photocatalytic activity of commercial TiO_2 co-doped with N and one metallic dopant (i.e., Al, Zn, Cr, Fe, Ni, or Cu) under simulated solar conditions for the degradation of azo dye in the aqueous environment.

3. EXPERIMENTAL METHODS

3.1. Materials and chemicals

The chemicals used in this study, with corresponding manufacturer sources and functions, are listed in **Table 3.1.**

Table 3.1. List of chemicals used in this study.

Chemical	Manufacturer source	Function
Titanium dioxide powder (TiO_2, ≥ 99%, ~20 nm), anatase:rutile ratio = 80:20	US Research Nanomaterials Inc.	Photocatalyst
Aluminum nitrate nonahydrate ($Al(NO_3)_3.9H_2O$, ≥ 98%)	Sigma Aldrich	Metallic dopant
Zinc nitrate hexahydrate ($Zn(NO_3)_2.6H_2O$, 98%)	Sigma Aldrich	Metallic dopant
Chromium(III) nitrate nonahydrate ($Cr(NO_3)_3.9H_2O$, 99%)	Sigma Aldrich	Metallic dopant
Iron(III) nitrate nonahydrate ($Fe(NO_3)_3.9H_2O$, ≥ 98%)	Sigma Aldrich	Metallic dopant
Nickel(II) nitrate hexahydrate ($Ni(NO_3)_2.6H_2O$)	Sigma Aldrich	Metallic dopant
Copper(II) nitrate trihydrate ($Cu(NO_3)_2.3H_2O$)	Sigma Aldrich	Metallic dopant
Triethylamine (TEA, $(C_2H_5)_3N$, ≥ 99%)	Sigma Aldrich	Non-metallic dopant
Direct Blue 71 (DB71, $C_{40}H_{23}N_7O_{13}S_4 \cdot 4Na$)	Sigma Aldrich	Dye
Nitric acid (HNO_3, 70%)	Sigma Aldrich	pH adjustment
Sodium hydroxide (NaOH, ≥ 97.0%, pellets)	Sigma Aldrich	pH adjustment

Isopropyl alcohol / 2-Propanol (IPA, ≥ 99.5%)	Sigma Aldrich	Radical scavenger
Ethylenediaminetetraacetic acid disodium salt dihydrate (EDTA-2Na)	Sigma Aldrich	Radical scavenger
L-Ascorbic acid (L-AA, 99%)	Sigma Aldrich	Radical scavenger
Dimethyl sulfoxide (DMSO, ≥ 99.9%)	Sigma Aldrich	Radical scavenger
Deionized water (DI water)	Milli-Q EQ 7000 system	

3.2. Direct Blue 71

Direct Blue 71 (DB71) is an anionic, water-soluble tri-azo dye composed of four naphthalene rings and sulfonate groups. Its chemical structure is described in **Figure 3.1**.

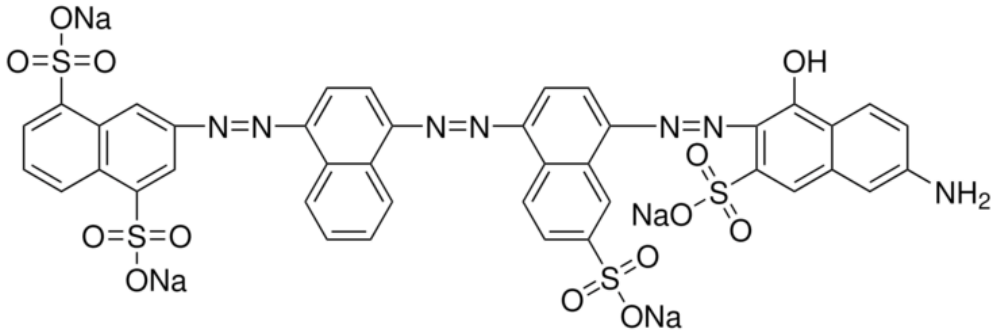

Figure 3.1. Chemical structure of DB71. [79]

3.3. Synthesis of doped TiO_2 photocatalysts

Metallic salts, including $Al(NO_3)_3.9H_2O$, $Zn(NO_3)_2.6H_2O$, $Cr(NO_3)_3.9H_2O$, $Fe(NO_3)_3.9H_2O$, $Ni(NO_3)_2.6H_2O$, and $Cu(NO_3)_2.3H_2O$ were used as the sources of Al, Zn, Cr, Fe, Ni, and Cu dopants in TiO_2, respectively.

1 g of TiO_2 was added to 20 mL of DI water, pre-sonicated for 1 min, and well stirred for 30 min. Two aqueous solutions containing 10 mL of TEA at 3 at. % (relative to Ti at.%) and 15 mL of each metallic salt at 2 at.% were separately prepared in two glass vials. These solutions were then thoroughly mixed with TiO_2 suspension for 30 min. The resultant mixture was subsequently dried in an oven at 80 ºC before being calcined at 350 ºC for 2 h. The final product is denoted as M,N-TiO_2 (where M = Al, Zn, Cr, Fe, Ni, or Cu).

To deconvolve the role of each dopant of the photocatalyst exhibiting the superior performance (i.e., Fe,N-TiO_2) on dye photodegradation, samples composed of TiO_2 and either $Fe(NO_3)_3.9H_2O$ (Fe-TiO_2) or TEA (N-TiO_2) were prepared following the aforementioned synthesis procedure. For comparison, pristine TiO_2 was also calcined at 350 ºC (denoted as TiO_2 350).

3.4. Characterization of TiO_2-based photocatalysts

The morphological structure and elemental composition of TiO_2-based photocatalysts were examined using a ThermoFisher Quattro S scanning electron microscope with energy-dispersive X-ray spectroscopy (SEM-EDX) for the investigation of elemental distribution. X-ray diffraction (XRD) patterns were obtained from Rigaku SmartLab X-ray diffractometer using focused Cu Kα radiation (Kα = 1.541 Å) through a continuous scanning process with a step width of 0.01° over the range of 20° to 80°. X-ray photoelectron spectroscopy (XPS) measurements were conducted using a Thermo-Fisher K-Alpha$^+$ XPS spectrometer equipped with an unmonochromated Al Kα (1486.6 eV) X-ray source, with a typical depth of analysis of approximately 5 nm. The zeta potentials of Fe,N-TiO_2 samples in the pH range of 4-8 were measured using a Zetasizer Nano DLS (Malvern Panalytical Ltd.), with a concentration of 1 mg of photocatalyst per 8 ml of DI water. The photoluminescent (PL) measurement was performed on the HORIBA Jobin Yvon Fluorolog-3 spectrofluorometer equipped with a Xenon lamp source to examine the recombination rate of photoinduced electron-hole pairs. The light absorption capacity and band gap of TiO_2-based photocatalysts were determined via a PerkinElmer Lambda 750 UV-vis-near-infrared spectrometer equipped with a 100 mm Spectralon InGaAs Integrating Sphere. Indeed, the optical band gap of each TiO_2-based sample was calculated from the optical spectral absorption using the Tauc equation:

$$(\alpha.h\nu)^{1/\gamma} = B(h\nu - E_g) \tag{3.1}$$

where h is the Planck constant, ν is the photon's frequency, E_g is the band gap energy, and B is a constant. The γ factor depends on the nature of the electron transition and is equal to 1/2 for direct transition band gaps and 2 for indirect transition band gaps, respectively. In this work, γ = 2, since we use commercial TiO_2 with predominantly anatase phase, which behaves as an indirect band gap semiconductor. [71] To obtain the value of α, we use the Kubelka-Munk function:

$$\alpha = F(R) = \frac{K}{S} = \frac{(1-R)^2}{2R} \tag{3.2}$$

where K and S are the absorption and scattering coefficients, respectively, and R is the reflectance of the material, which is obtained from the UV-Vis Diffuse Reflectance Spectroscopy (UV-Vis DRS). Substituting F(R), $E = h\nu$, and γ = 2 into the equation 3.1:

$$(F(R).E)^{1/2} = B(h\nu - E_g) \quad (3.3)$$

The band gap energy (E_g) is determined through the x-axis intersection of the linear fit of the Tauc plot. [80]

3.5. Evaluation of Direct Blue 71 (DB71) removal of TiO_2-based photocatalysts

3.5.1. Standard calibration curve of DB71 solutions

Characteristic peak of DB71: The DB71 solution was prepared at a concentration of 20 ppm. The highest absorbance observed in the UV-Vis spectra was at the wavelength of 586 nm (**Figure 3.2(a)**).

Calibration curve of DB71 solution: DB71 solutions were prepared at precise concentrations of 2.5, 5, 7.5, 10, 15, 20, and 25 ppm. After determining the respective absorbance at the wavelength of 586 nm, a standard curve for the dependence of dye concentration on the absorbance was created (**Figure 3.2(b)**).

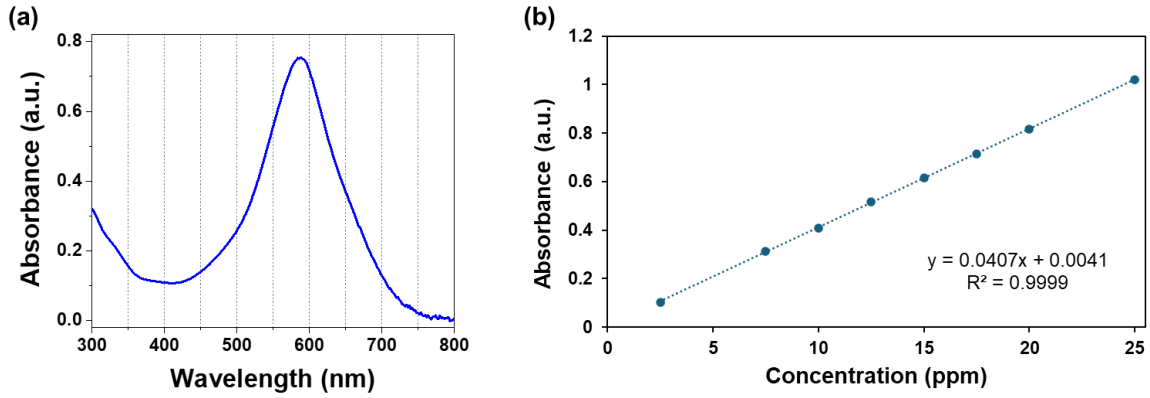

Figure 3.2. Characteristic peak (a) and standard calibration curve (b) of DB71 solution.

3.5.2. DB71 removal experiments

a. Design of the photocatalytic system: Reactions were carried out in a 250-mL glass beaker and stirred at a constant speed, with the temperature being controlled at approximately 20 °C. The light source was the Sol1A solar simulator system (Newport Corporation) with the illumination output power of 1 SUN (i.e., 1000 W/m^2), representing the amount of solar radiation received at the Earth's surface on a clear day around solar noon. [81] The distance

between the light source and the surface of the photocatalyst-dye suspension is maintained at a fixed ~15 cm.

b. Effects of dopants on the removal of DB71 in dark conditions: 0.05 g of each material (i.e., commercial TiO_2, TiO_2 350, M,N-TiO_2, Fe-TiO_2, and N-TiO_2 photocatalysts) was added to 100 mL of DB71 at a concentration of 20 ppm with an initial pH of approximately 6. The mixture was stirred in dark conditions for 2 h before being centrifuged. The DB71 concentration was determined using UV-Vis measurements after interpolation from the standard calibration curve of DB71. The removal efficiency (X %) of DB71 was calculated using the equation:

$$X\ (\%) = \frac{C_o - C_f}{C_o} \times 100\% \qquad (3.4)$$

where C_o and C_f (ppm) are the initial and final concentrations of DB71, respectively.

c. Effects of dopants on the removal of DB71 under solar irradiation: 0.05 g of each material (i.e., commercial TiO_2, TiO_2 350, M,N-TiO_2, Fe-TiO_2, and N-TiO_2 photocatalysts) was added to 100 mL of DB71 at a concentration of 20 ppm with an initial pH of approximately 6. The mixture was stirred in dark conditions for 30 min to reach equilibrium before exposure to solar irradiation for 2 h. The DB71 concentration was determined using UV-Vis measurements after interpolation from the standard calibration curve of DB71. The removal efficiency (X %) of DB71 was calculated via the equation (3.1).

d. Effect of pH conditions on the DB71 removal: Two separate experiments were conducted using the photocatalyst with the highest DB71 photodegradation efficiency (i.e., Fe,N-TiO_2) for each pH value, ranging from 3 to 8, in dark conditions and under solar irradiation. HNO_3 and NaOH 0.05 M were used for pH adjustment. 0.02 g of Fe,N-TiO_2 was added to 100 mL of DB71 at a concentration of 20 ppm with a specific pH value. The experimental procedures followed the two procedures described in the 3.4.2 (b) and 3.4.2 (c) sections. The experiment at each pH value was conducted thrice.

e. Radical scavenging tests: Scavengers are (in)organic compounds that deactivate specific radicals from participating in oxidative processes by reacting with them to form stable species that do not disrupt the reactions. [82] The scavenging study was performed to deconvolve the role of photogenerated radicals in the photocatalytic degradation of DB71 of Fe,N-TiO_2. The reaction was carried out in a similar way to the photocatalytic experiment described in the 3.4.2 (c) part but with the addition of either IPA (10% v/v), EDTA-2Na (0.01

M), L-ascorbic acid (L-AA, 0.1 mM), or DMSO (10 mM), which are used as scavengers for the photoinduced hydroxyl radicals ($^{\bullet}OH$), holes (h^+), singlet oxygen ($^1O_2$), and electrons (e^-), respectively. [83, 84] Each radical scavenging test was conducted thrice.

f. Time-dependent DB71 removal performance: 0.02 g of Fe,N-TiO_2 was added to 100 mL of DB71 at a concentration of 20 ppm with the optimal pH determined from 3.4.2. (d) experiment. The mixture was stirred in dark conditions for 30 min to reach the equilibrium conditions before being exposed to solar irradiation over a specific time interval. This was followed by centrifugation, UV-Vis measurement, and determination of the DB71 concentration in the solution. The experiment was repeated three times. In addition, we can calculate the kinetic constant of DB71 photodegradation from the obtained results, as the photodegradation of dyes is considered to follow pseudo-first-order kinetics (equation 3.5). [5, 85]

$$\frac{dC_t}{dt} = k_d\, C_t \tag{3.5}$$

where C_t (ppm) is the concentration of DB71 in the solution at the time t, and k_d (min^{-1}) is the kinetic constant of DB71 photodegradation.

4. RESULTS AND DISCUSSION

4.1. Effects of dopants on the removal of DB71

As seen from **Figure 4.1**, TiO_2 calcined at 350 ºC demonstrated an indirect band gap of ~3.16 eV, demanding stimulation from UV light. Meanwhile, introducing impurities into the TiO_2 lattice effectively decreased this value, enabling greater utilization of the solar light. In particular, the lowest band gap energy was found in Cr,N-TiO_2 and Fe,N-TiO_2 (~3.02 eV), while that of Zn,N-TiO_2 showed the least narrowing effect (~3.12 eV).

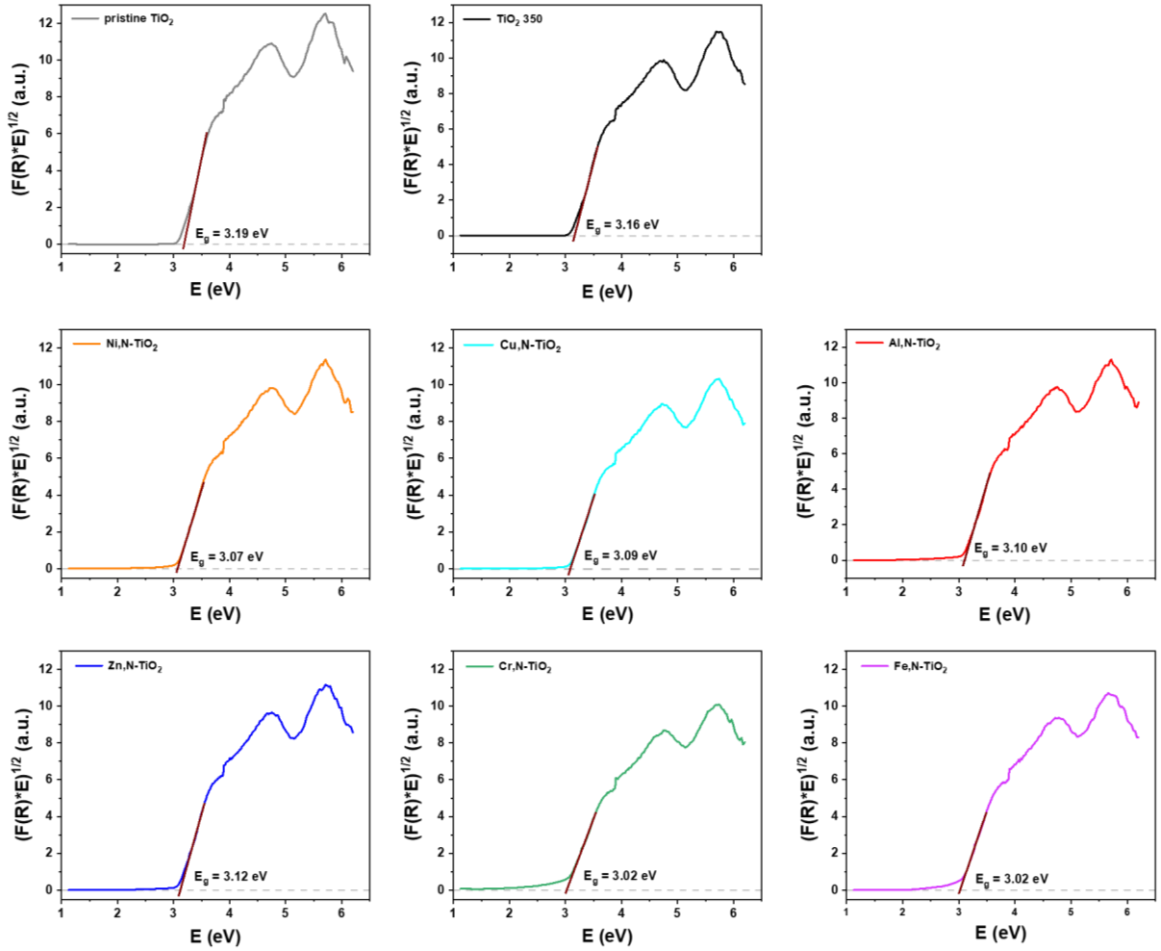

Figure 4.1. Band gap determination of pristine TiO_2, TiO_2 350, and M,N-TiO_2 photocatalysts (M = Al, Zn, Cr, Fe, Ni, and Cu).

Figure 4.2 illustrates the DB71 removal capacities of pristine TiO_2, TiO_2 350, and metal/N co-doped TiO_2. The inertness of DB71 under solar illumination was observed due to the recalcitrance of the azo groups, as only ~3% of DB71 was photolyzed. As-received TiO_2 exhibited limited adsorption capacity (8.27 $\pm$ 0.17%) and modest photodegradation efficiency (61.90 $\pm$ 4.15%) of DB71. Meanwhile, TiO_2 calcined at 350 ºC exhibited a slight decrease in DB71 removal efficiencies in both dark and solar-illuminated conditions compared to pristine

TiO_2. This was likely due to the sintering effect of nanoparticles during thermal treatment, which led to the agglomeration of TiO_2 350 particles, thus reducing their active surface area. [86]

The introduction of all binary dopant sets enhanced the DB71 adsorption efficiencies of co-doped TiO_2, indicating an increased surface area of TiO_2, which aligns with the results obtained in previous literature. [85, 87-92] This factor favorably promoted the corresponding photocatalytic performances to different extents except for Cu,N-TiO_2. Of note, the system based on Fe,N-TiO_2 demonstrates the highest DB71 degradation under solar illumination.

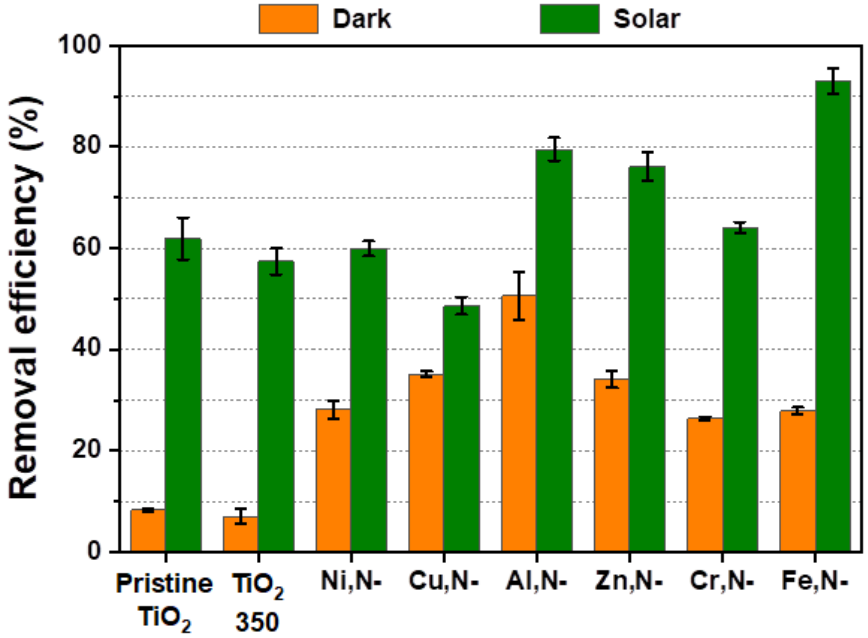

Figure 4.2. DB71 removal efficiencies of pristine TiO_2, TiO_2 350, and M,N-TiO_2 (M = Al, Zn, Cr, Fe, Ni, and Cu) [m_{cat} = 0.5 g/L, C_{0_DB71} = 20 ppm, pH = ~6].

To further elucidate the photocatalytic performances of M,N-TiO_2 samples, ultraviolet-visible diffuse reflectance spectroscopy (UV–Vis DRS) and photoluminescence (PL) measurements were employed to investigate the light-harvesting behavior and the recombination rate of photogenerated electron-hole pairs, respectively (**Figures 4.3(a)** – **(b)**). TiO_2 doped with Ni/N and Cu/N exhibited suppressed photogenerated charge carriers and a slight improvement in visible light harvesting capacity. However, the thicker adsorbed dye layer (**Figure 4.2**) might impede light penetration to the active sites of the photocatalyst, leading to ineffective degradation of DB71 under solar illumination. In contrast, Al,N-TiO_2, possessing the highest adsorption efficiency of DB71 (~50%), demonstrated better visible-light utilization along with improved photogenerated charge carrier separation, thereby removing roughly 80% of DB71 when illuminated by solar light. Meanwhile, the DB71 photodegradation

capability of Zn,N-TiO_2 was lower, with remarkably high PL intensity despite its great absorption capability in the visible light region. This may result from an overabundance of dopants due to the difference in the substitution level (i.e., extent of TiO_2 lattice distortion), which serves as the recombination center, thereby emphasizing the critical importance of optimizing doping element concentrations. [93] Although Cr,N-TiO_2 exhibited a considerably high visible light harvesting capacity and the lowest recombination rate of e^-/h^+, the DB71 photodegradation performance of this sample was unimpressive. One possible explanation is that the energy levels introduced by doped Cr may not align well with the conduction and valence bands of TiO_2, which hinders the efficient transfer of electrons to the CB or holes to the VB and, consequently, the formation of reactive radical species, thereby impacting overall photocatalytic activity. It is noteworthy that TiO_2 co-doped with Fe and N displayed the highest visible light absorption and significantly low PL intensity (i.e., low e-/h+ recombination rate), which accounted for its highest DB71 removal efficiency of over 93% under solar illumination (**Figure 4.2**).

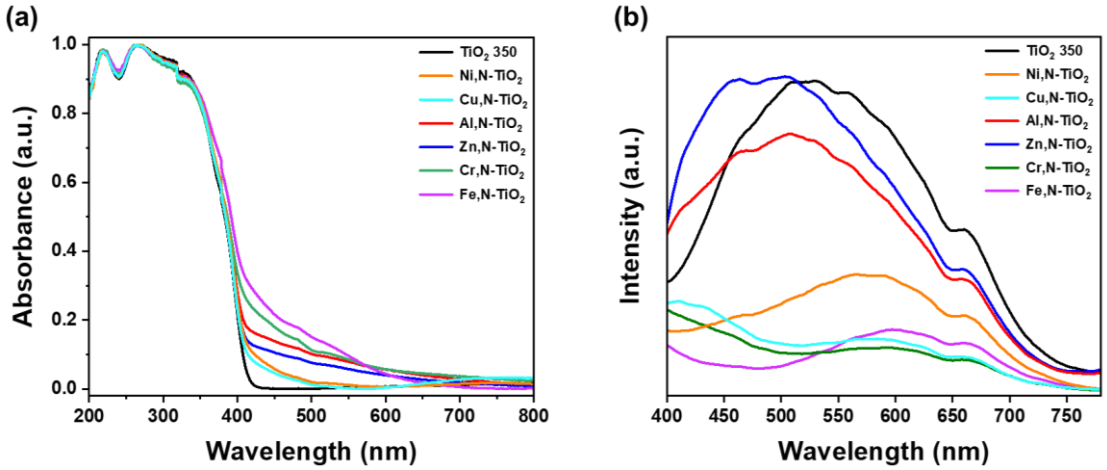

Figure 4.3. UV-Vis DRS (a) and PL (b) results of TiO_2 350 and M,N-TiO_2 (M = Al, Zn, Cr, Fe, Ni, and Cu).

Figure 4.4 compares the DB71 removal efficiencies of TiO_2 350, N-TiO_2, Fe-TiO_2, and Fe,N-TiO_2 in order to study the contributions of each dopant to the superior photocatalytic performance of Fe,N-TiO_2. Despite a marginal rise in visible-light absorption capacity (**Figure 4.3**), the DB71 photodegradation of TiO_2 deteriorated with the presence of solely N dopant, which trend was also reported in the study of Irie et al. [94] This is due to the isolated, narrow N *2p* state situated above the valence band, which partially traps and prevents photogenerated electrons from reaching the conduction band, thereby reducing the photogenerated current. [26, 94] Meanwhile, a substantial amount (~84.5 %) of DB71 was removed by TiO_2 doped with

Fe^{3+} under solar illumination. The Fe^{3+} dopant has been shown to create a shallow charge trap within the TiO_2 lattice, promoting interfacial charge transfer processes that are advantageous for separating photoinduced electron-hole pairs and reducing the band gap of TiO_2 ($E_g \approx 3.04$ eV). [29, 92, 95]

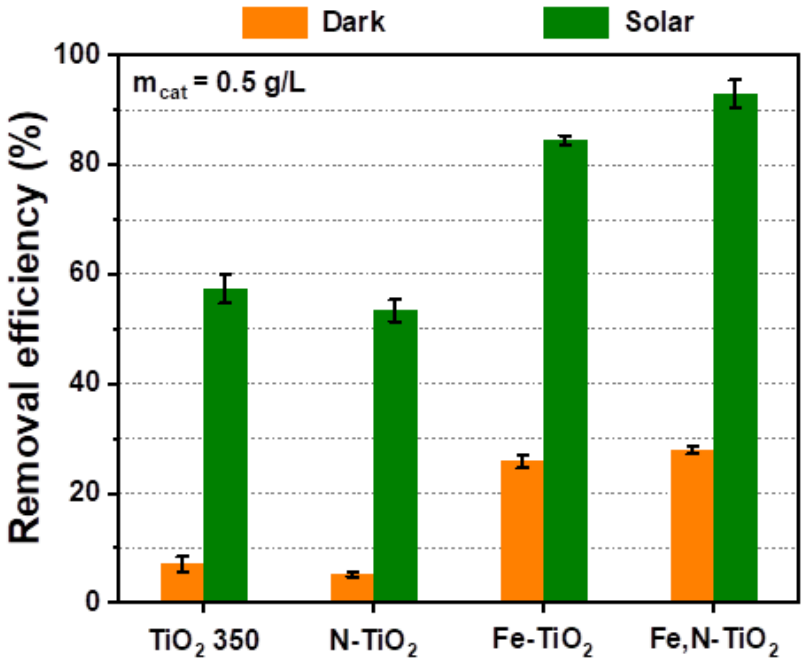

Figure 4.4. DB71 removal efficiencies of TiO_2 350, N-TiO_2, Fe-TiO_2, and Fe,N-TiO_2 [m_{cat} = 0.5 g/L, C_{0_DB71} = 20 ppm, pH = ~6].

The synergistic effect of Fe and N dopants was observed in the enhanced photodegradation performance of Fe,N-TiO_2 for DB71, compared to single Fe- or N-doped TiO_2, attributed to a greater dye photodegradation efficiency, visible-light harvesting capacity, and inhibition of electron-hole recombination during irradiation (**Figure 4.5**).

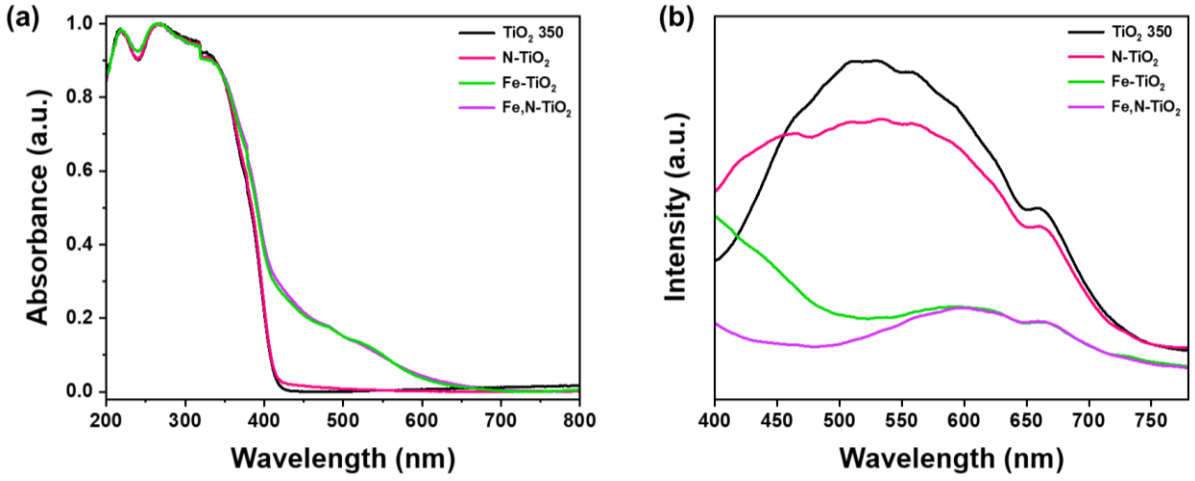

Figure 4.5. UV-Vis DRS (a) and PL (b) results of TiO_2 350, N-TiO_2, Fe-TiO_2, and Fe,N-TiO_2.

4.2. Characterization of Fe,N-TiO_2 photocatalyst

TiO_2 calcined at 350 ºC exhibited an aggregated particle network, while no significant morphological changes were noticed when Fe and N were co-introduced into TiO_2, as shown in **Figures 4.6 (a) and (b)**. The uniform distribution of the composition of Fe,N-TiO_2 was also observed (**Figure 4.6 (c)**).

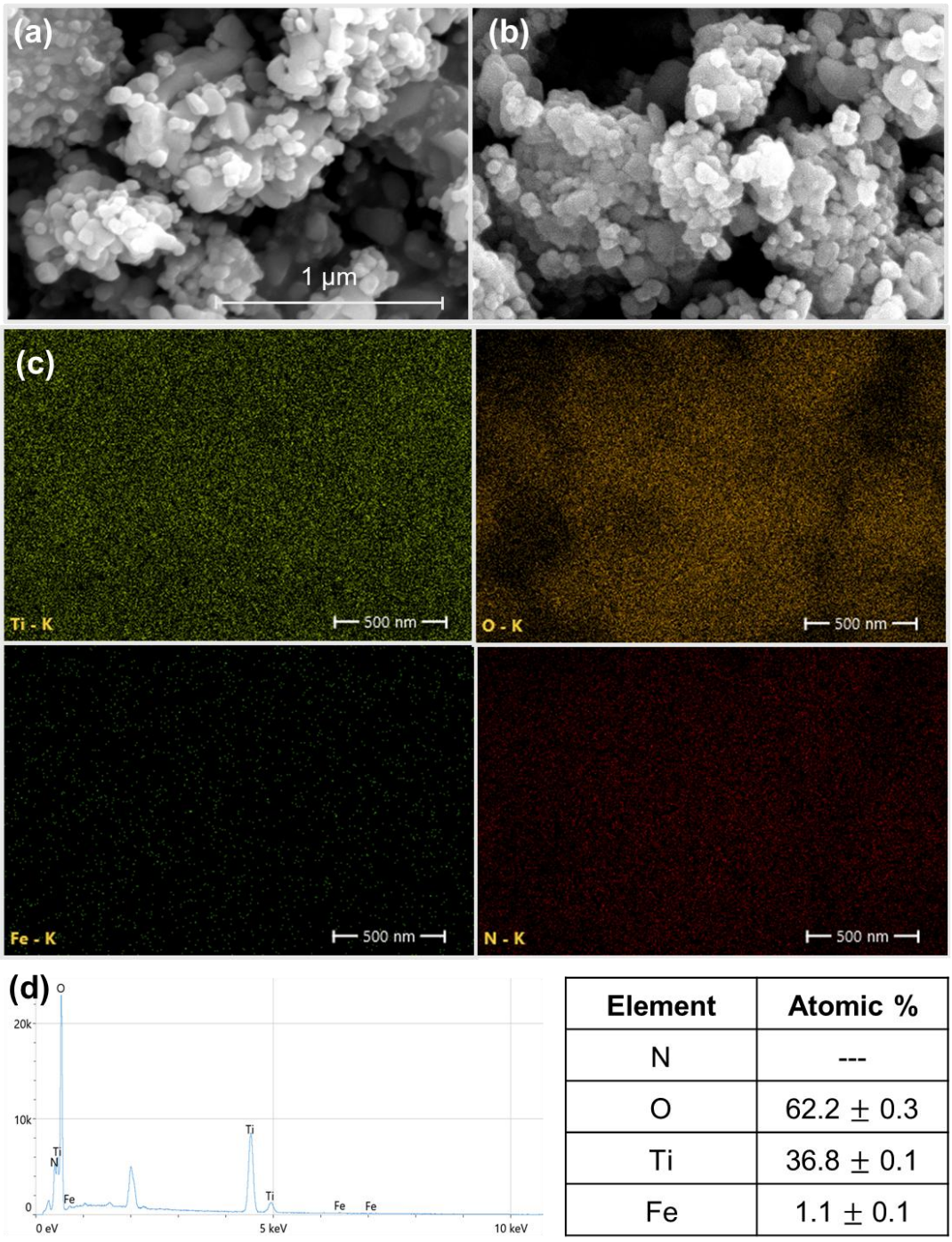

Element	Atomic %
N	---
O	62.2 ± 0.3
Ti	36.8 ± 0.1
Fe	1.1 ± 0.1

Figure 4.6. SEM images of TiO_2 350 (a) and Fe,N-TiO_2 (b), and EDX color mapping (c) and EDX spectrum (d) of Fe,N-TiO_2.

XRD analysis was conducted to investigate the change in crystallinity of TiO_2 after being modified with Fe/N. As shown in **Figure 4.7**, characteristic peaks of anatase (i.e., 2θ = 25.3°, 37.8°, 48.1°, 53.9°, 62.7°, 69.0°, and 70.3°) and rutile (2θ = 27.4°, 36.1°, 41.2°, 54.3°, 56.6°, and 64.0°) phases were observed in the XRD pattern of TiO_2 350. [96] Regarding Fe,N-TiO_2 sample, all the aforementioned peaks experienced marginal shifts toward larger angles. This indicated the contraction within the TiO_2 crystal lattice due to the presence of Fe^{3+} ions with a smaller ionic radius (~6.4 pm) compared to that of Ti^{4+} (~6.8 pm). [97]

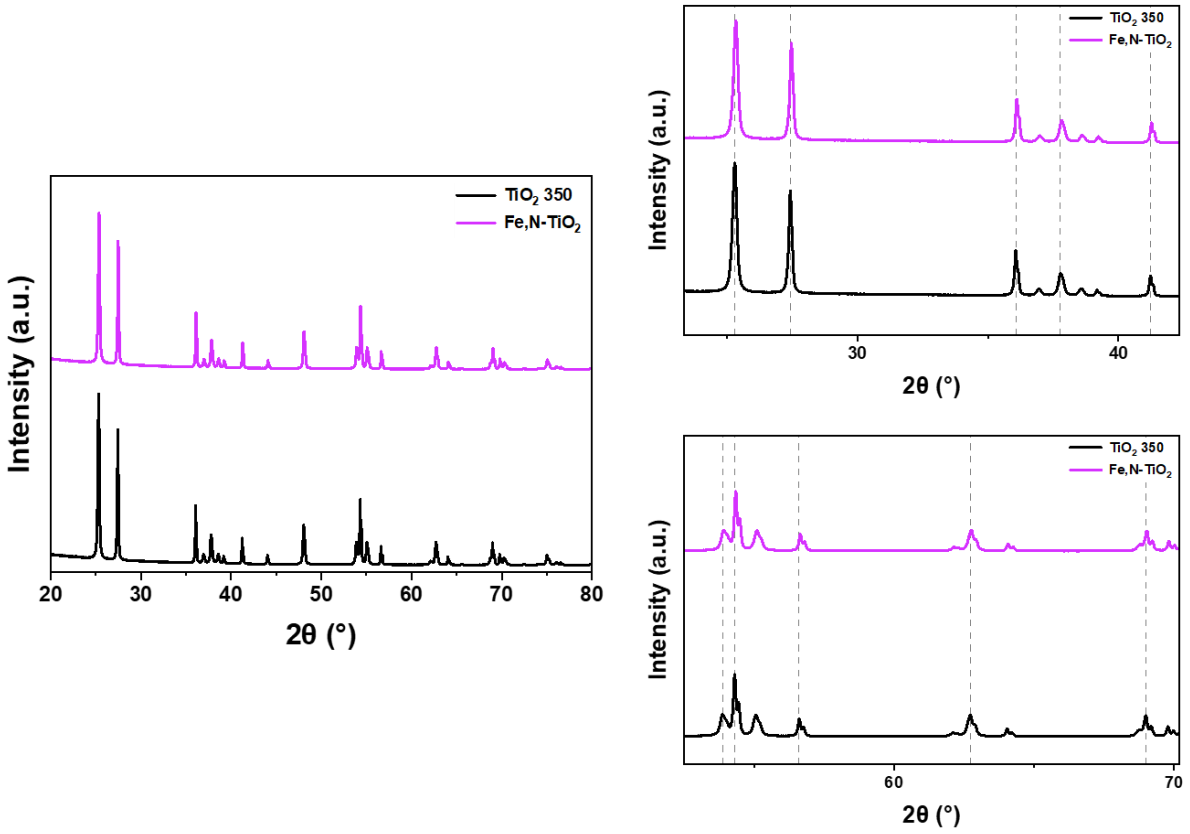

Figure 4.7. XRD patterns of TiO_2 350 and Fe,N-TiO_2.

The elemental composition and chemical state of photocatalysts can be inspected via the surface-sensitive XPS technique. Regarding the XPS Ti 2p spectra (**Figure 4.8(a)**), two characteristic peaks at 464.15 eV and 458.44 eV observed in the TiO_2 350 plot were assigned to Ti $2p_{1/2}$ and Ti $2p_{3/2}$, respectively. [98] When incorporating Fe and N elements into the TiO_2 lattice, these peaks underwent a noticeable drop in their intensities, as a result of the substitution of dopants for Ti atoms in the lattice, and were displaced to lower binding energies, indicating the partial reduction of Ti^{4+}. Of note, the TiO_2 lattice might compensate for the charge imbalance (since Ti^{4+} ions were partly replaced with Fe^{3+}) and neutralize the excess electrons introduced by N by forming oxygen vacancies (OVs). OVs reduce the electron density around

the remaining O atoms, increasing their corresponding binding energy. This could be clarified from the deconvoluted XPS O 1s spectra of TiO_2 350, where two peaks at 529.46 eV (O lattice) and 530.38 eV (Ti-OH) were noticed [99], with the latter broadening and shifting to higher binding energy (i.e., 530.88 eV) with the presence of Fe and N impurities. Notably, the formation of OVs could be considered one of the factors effectively promoting the photodegradation of organic compounds, including this work, as they create localized electron-rich defect sites that facilitate electron transport and suppress charge carrier recombination. [100-102] Moreover, the appearance of a shoulder at ~529.34 eV in Fe,N-TiO_2 sample might be the outcome of new oxygen bonding configurations such as Ti–O–Fe, Ti–O–N, and Fe–O–N.

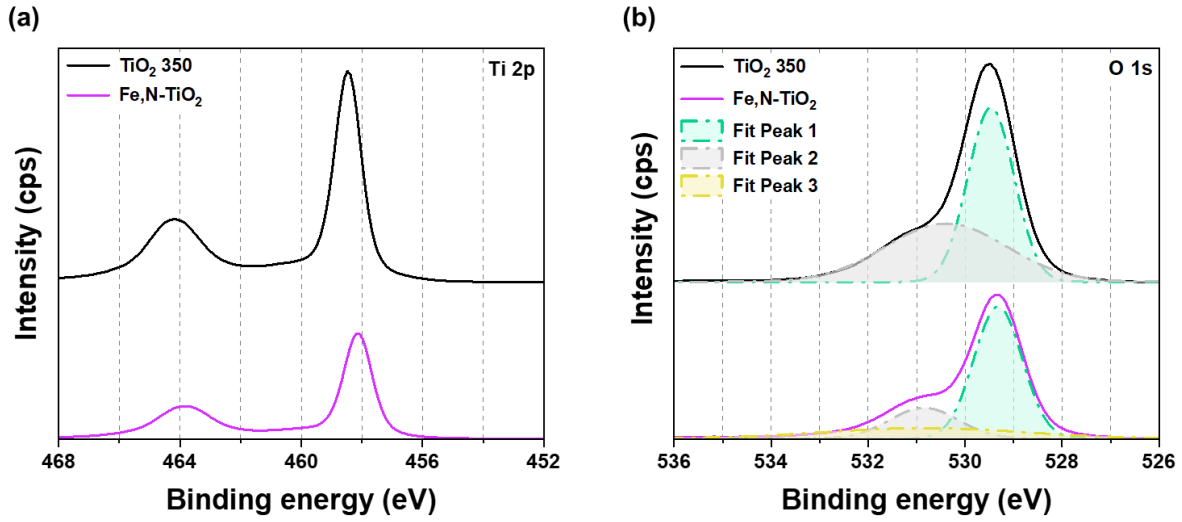

Figure 4.8. XPS spectra of Ti 2p (a) and O 1s (b) of TiO_2 350 and Fe,N-TiO_2.

The pH value at which the net surface charge of a solid material is equivalent to zero (i.e., the point of zero charge, pH_{pzc}) can be determined through zeta potential measurement. As shown in **Figure 4.9**, pH_{pzc} of Fe,N-TiO_2 was approximately 5.46, meaning that the catalyst surface was positively charged at pH values lower than 5.46 and vice versa.

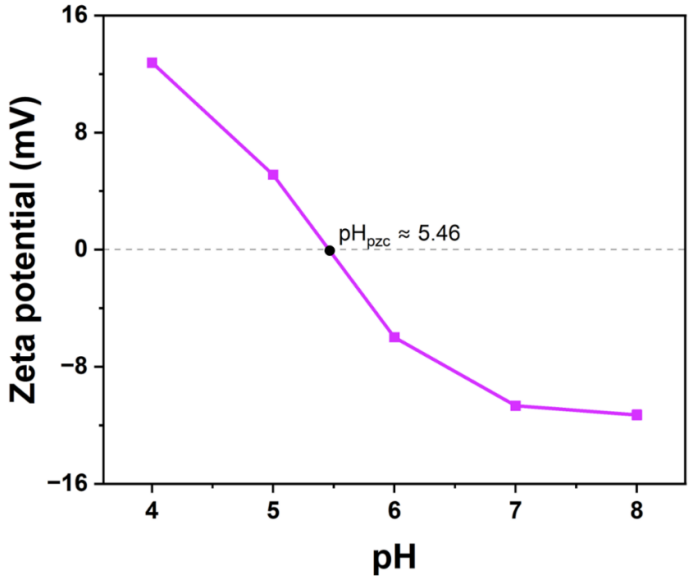

Figure 4.9. Zeta potentials of Fe,N-TiO_2 in the pH range from 4 to 8.

4.3. DB71 removal performance of Fe,N-TiO_2 photocatalyst

Since the removal efficiency of DB71 under solar illumination using 0.5 g/L of Fe,N-TiO_2 without adjusting any operating parameters exceeded 93%, further investigation was carried out with a catalyst content of 0.2 g/L to optimize the photocatalytic performance.

4.3.1. Radical scavenging tests

Scavengers are (in)organic compounds used to deactivate specific radicals from participating in oxidative processes by reacting with them to form stable species that do not disrupt the reactions. [82] Radical scavenging tests were conducted to elucidate the main contributor among photogenerated radicals to the photocatalytic removal of DB71 (**Figure 4.10**). IPA (10% v/v), EDTA-2Na (0.01 M), L-AA (0.1 mM), or DMSO (10 mM) were added to capture $^{\bullet}OH$, h^+, $^1O_2$, and e^-, respectively. The DB71 photodegradation efficiency of Fe,N-TiO_2 without scavengers was 66.37 ± 2.45%. However, it was suppressed to ~11% with the presence of EDTA-2Na, presenting the most significant impact exerted by photogenerated h^+. Besides, $^1O_2$ also played a crucial role in the photodegradation of DB71 of Fe,N-TiO_2, as only ~38% of DB71 was removed when L-AA was added to the solution mixture. Nevertheless, adding IPA and DMSO resulted in slight increases in DB71 removal efficiency, indicating hindrance from $^{\bullet}OH$ and e^-.

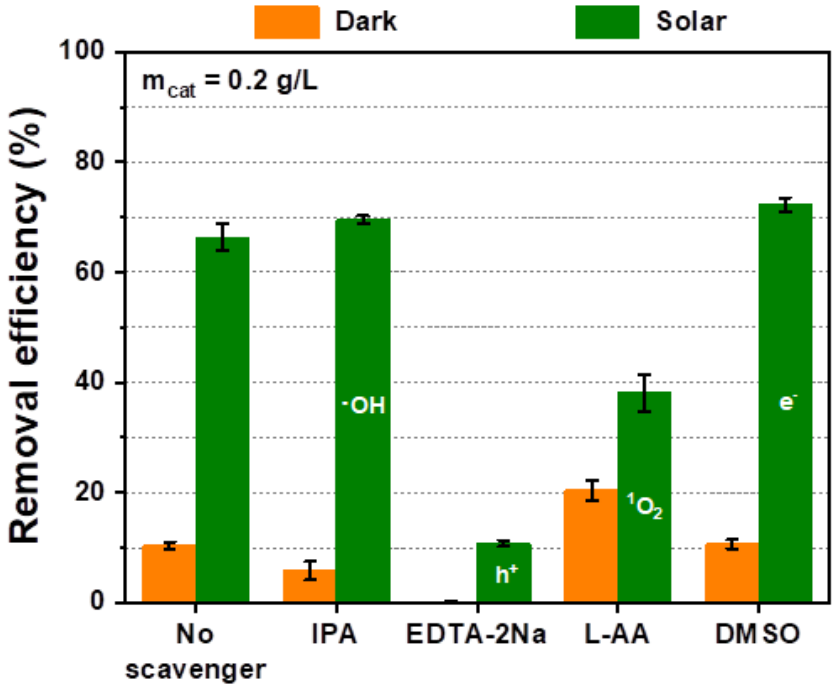

Figure 4.10. Radical scavenging tests of Fe,N-TiO_2 [m_{cat} = 0.2 g/L, C_{0_DB71} = 20 ppm, pH = ~6].

4.3.2. Effect of pH conditions on the DB71 removal

Figure 4.11 illustrates the removal efficiencies of DB71 by Fe,N-TiO_2 at varying pH conditions. At the initial pH of ~6, approximately 10.4% and 66.4% of DB71 were removed by Fe/N-doped TiO_2 under dark and solar-illuminated conditions, respectively. Tuning the environment to be more acidic favors the electrostatic interaction between anionic DB71 molecules and positively charged Fe,N-TiO_2 ($pH_{pzc} \approx 5.46$), leading to a higher DB71 adsorption capacity. Nonetheless, the adsorbed dye partly blocked or absorbed the incoming light, reducing the light intensity that reached the active sites of the photocatalyst. [103] Meanwhile, Fe,N-TiO_2 underwent a decline in the overall DB71 removal efficiency in an alkaline environment. Apart from the dye-photocatalyst repulsion, this was mostly due to the partial consumption of photogenerated h^+, the primary contributor to dye photodegradation, by introduced OH^- to form •OH impediment (Equation 2.7). [104] Noticeably, the photodegradation efficiency of Fe,N-TiO_2 peaked at neutral pH, underscoring the redundancy of chemical additions for pH adjustment in real wastewater systems.

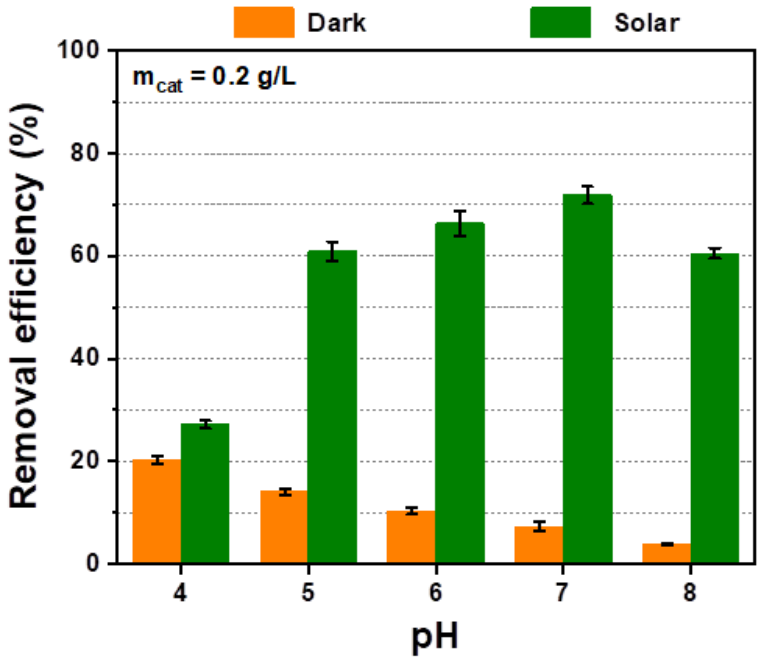

Figure 4.11. Effect of pH conditions on the DB71 removal by Fe,N-TiO_2 [m_{cat} = 0.2 g/L, C_{0_DB71} = 20 ppm].

4.3.3. Time-dependent DB71 removal performance

Figure 4.12(a) illustrates the DB71 removal performance of Fe,N-TiO_2 over time. With a photocatalyst content of 0.2 g/L and a pH value of ~7, less than 8% of DB71 was removed during a 5-hour adsorption period. In contrast, under similar conditions, the performance with solar illumination reached 91.22 ± 1.52%. Calculated from these results, the dye photodegradation in this study also followed pseudo-first-order kinetics, with a kinetic constant of 0.007 min^{-1}. (**Figure 4.12 (b)**).

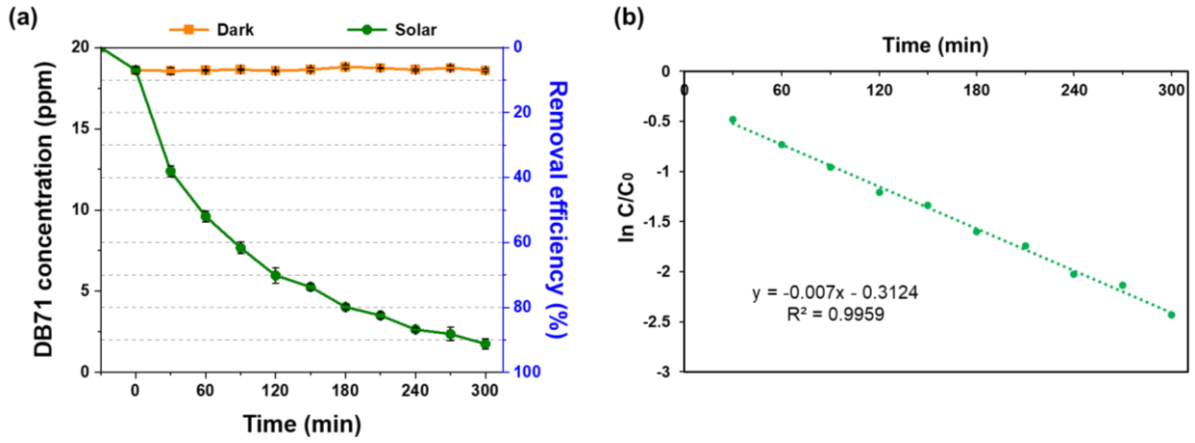

Figure 4.12. DB71 removal performance of Fe,N-TiO_2 with respect to time (a), and determination of the kinetic constant of DB71 photodegradation by Fe,N-TiO_2. [m_{cat} = 0.2 g/L, C_{0_DB71} = 20 ppm, pH = ~7].

5. CONCLUSION

In this study, commercial TiO_2 photocatalysts were modified with binary dopants, nitrogen and a metal element (Al, Zn, Cr, Fe, Ni, or Cu). Their photocatalytic performances under simulated solar irradiation, including their light absorption behaviors, recombination rates of charge carriers, and photodegradation efficiency of DB71 in the aqueous environments, were extensively investigated. The quantity and electronic band structure of dopants were noticed to be of paramount importance in the resulting photocatalytic behaviors. Fe,N-TiO_2 significantly absorbed incoming visible light to generate holes and electrons with a low recombination rate, thereby most effectively degrading over 90% of DB71 at the initial dye concentration of 20 ppm in 2 h with a photocatalyst content of 0.5 g/L. The DB71 photodegradation of Fe,N-TiO_2 sample was primarily attributed to the photogenerated holes, followed by singlet oxygen radicals. The study also investigated that pH~7 was the optimal pH for DB71 degradation by Fe/N-doped TiO_2.

NOTABLE ACHIEVEMENTS

During my studies at the University of Oklahoma, I have had the honor of participating in four publications:

- First author of the article: **Nguyen, V.H.T.**, Nguyen, V., Popy, D., Tran, H.M., Bui, N.T., 2025. Solar-driven Direct Blue 71 dye decontamination with metal- and non-metal-doped titanium dioxide photocatalyst. (*in-prep work*)

- Co-first author of three articles:

1. Meissner, M.S., **Nguyen, V.H.T.**, Bousrih, I., Le, V.T.C., Frickenstein, A., Le, G.V. and Bui, N.T., 2023. Thermodynamic insights into selenium oxyanion removal from synthetic flue gas desulfurization wastewater with temperature-swing solvent extraction. *Frontiers in Chemistry*, *11*, p.1225843.

2. Le, V.T.C., **Nguyen, V.H.T.**, Bui, N.T., 2025. Melamine-based porous polymer network adsorbent beads for selective separation of platinum group metals from multicomponent aqueous streams. *Journal of Polymers.* (*under review*)

3. **Nguyen, V.H.T.**, Tran, H.M., Bui, N.T., 2025. Low-cost functionalized carbon nanotube adsorbents for chromate removal from contaminated water environments. (*in-prep work*)

I participated in the North American Membrane Society (NAMS) 2024 Conference (Santa Fe, New Mexico) and the Great Plains Catalysis (GPCS) 2024 conference in Norman, Oklahoma, where I presented a poster on the topic of "Solar-driven dye decontamination with metal- and non-metal-doped titanium dioxide photocatalysts." Moreover, I had the opportunity to get trained at the Lawrence Berkeley National Laboratory for seven weeks and attend the Annual User Meeting 2023 there. I was also fortunate to be awarded the Dolese Fellowship for the 2023-2024 school year.

REFERENCES

1. Al-Tohamy, R., S.S. Ali, F. Li, K.M. Okasha, Y.A.-G. Mahmoud, T. Elsamahy, H. Jiao, Y. Fu, and J. Sun, A critical review on the treatment of dye-containing wastewater: Ecotoxicological and health concerns of textile dyes and possible remediation approaches for environmental safety, Ecotoxicology and environmental safety. 231: pp. 113160, 2022.

2. de Campos Ventura-Camargo, B. and M.A. Marin-Morales, Azo dyes: Characterization and toxicity-a review, Textiles and Light Industrial Science and Technology. 2(2): pp. 85-103, 2013.

3. Bafana, A., S.S. Devi, and T. Chakrabarti, Azo dyes: Past, present and the future, Environmental Reviews. 19(NA): pp. 350-371, 2011.

4. Benkhaya, S., S. M'rabet, and A. El Harfi, Classifications, properties, recent synthesis and applications of azo dyes, Heliyon. 6(1), 2020.

5. Viswanathan, B., Photocatalytic degradation of dyes: An overview, Current Catalysis. 7(2): pp. 99-121, 2018.

6. Crini, G. and E. Lichtfouse, Advantages and disadvantages of techniques used for wastewater treatment, Environmental chemistry letters. 17: pp. 145-155, 2019.

7. Yuan, X., C. Zhou, Y. Jin, Q. Jing, Y. Yang, X. Shen, Q. Tang, Y. Mu, and A.-K. Du, Facile synthesis of 3D porous thermally exfoliated g-C_3N_4 nanosheet with enhanced photocatalytic degradation of organic dye, Journal of Colloid and Interface Science. 468: pp. 211-219, 2016.

8. Liu, D., C. Jin, F. Shan, J. He, and F. Wang, Synthesizing $BaTiO_3$ nanostructures to explore morphological influence, kinetics, and mechanism of piezocatalytic dye degradation, ACS applied materials & interfaces. 12(15): pp. 17443-17451, 2020.

9. Hanh, N.T., D. Van Thuan, N.M. Khai, P.T. Thuy, T.T.M. Hang, N.H.T. Vy, N. Van Noi, D.T. Tran, T.D. Pham, and N.T.T. Truc, Synthesis of Co_3O_4 coated on N, S doped TiO_2 for novel photocatalytic degradation of toxic organic pollutant in aqueous environment, Ceramics International. 46(13): pp. 21610-21616, 2020.

10. Ullah, H., Z. Khan, J.A. Nasir, T. Balkan, I.S. Butler, S. Kaya, and Z.U. Rehman, Green synthesis of mesoporous MoS_2 nanoflowers for efficient photocatalytic degradation of Congo red dye, Journal of Coordination Chemistry. 74(14): pp. 2302-2314, 2021.

11. Jiang, H., J. He, C. Deng, X. Hong, and B. Liang, Advances in Bi_2WO_6-based photocatalysts for degradation of organic pollutants, Molecules. 27(24): pp. 8698, 2022.

12. Liu, Y., H. Wan, M. Islam, K.F. Hasan, S. Cao, Z. Wang, Y. Xiong, S. Lü, H. Liu, and S. Mahmud, Liquid exfoliated Bi_2S_3 nanosheets as photocatalysts for degradation of azo dyes and detoxification of hexavalent chromium, Materials Science and Engineering: B. 285: pp. 115898, 2022.

13. Prabagar, J.S., T. Tenzin, S. Yadav, K.M.A. Kumar, and H.P. Shivaraju, Facile synthesis of $NdFeO_3$ perovskite for photocatalytic degradation of organic dye and antibiotic, Materials Today: Proceedings. 75: pp. 15-23, 2023.

14. Bhagwat, U.O., M.C. Maridevaru, A. Al Souwaileh, J.J. Wu, and S. Anandan, Layered Perovskite $La_2Ti_2O_7$ Nanostructures for Photocatalytic Degradation of Congo Red Dye Pollutant, ChemistrySelect. 9(41): pp. e202403511, 2024.

15. Kumar, E.V., C.M. Swamy, H.A. Rao, M. Shashank, K. Deepa, G. Suma, M.N. Rani, and G. Nagaraju, Facile green synthesis of $CuWO_4$ nanoparticles and its application for the photocatalytic degradation of rose Bengal dye under visible light irradiation, Inorganic Chemistry Communications. 172: pp. 113706, 2025.

16. Backes, C.W., F.B. Reis, G.B. Strapasson, M. Assis, E. Longo, and D.E. Weibel, Green synthesis of carbon quantum dots for enhancing photocatalytic activity: Hydrogen/oxygen evolution and dye photodegradation, Catalysis Today. 443: pp. 114996, 2025.

17. Nguyen, V.N., D.T. Tran, M.T. Nguyen, T.T.T. Le, M.N. Ha, M.V. Nguyen, and T.D. Pham, Enhanced photocatalytic degradation of methyl orange using ZnO/graphene oxide nanocomposites, Research on Chemical Intermediates. 44: pp. 3081-3095, 2018.

18. Armaković, S.J., M.M. Savanović, and S. Armaković, Titanium dioxide as the most used photocatalyst for water purification: An overview, Catalysts. 13(1): pp. 26, 2022.

19. Bakar, F.A. and N.S.I.M. Foad, Synthesis of TiO_2 photocatalyst with tunable optical properties and exposed facet for textile wastewater treatment, Results in Optics. 13: pp. 100545, 2023.

20. Wang, L. and J. Yu, *Principles of photocatalysis*, in *Interface science and technology*. 2023, Elsevier. p. 1-52.

21. Dashora, A., N. Patel, D. Kothari, B. Ahuja, and A. Miotello, Formation of an intermediate band in the energy gap of TiO_2 by Cu–N-codoping: First principles study and experimental evidence, Solar energy materials and solar cells. 125: pp. 120-126, 2014.

22. Singaram, B., J. Jeyaram, R. Rajendran, P. Arumugam, and K. Varadharajan, Visible light photocatalytic activity of tungsten and fluorine codoped TiO_2 nanoparticle for an efficient dye degradation, Ionics. 25: pp. 773-784, 2019.

23. Zaleska, A., Doped-TiO_2: A review, Recent patents on engineering. 2(3): pp. 157-164, 2008.

24. Basavarajappa, P.S., S.B. Patil, N. Ganganagappa, K.R. Reddy, A.V. Raghu, and C.V. Reddy, Recent progress in metal-doped TiO_2, non-metal doped/codoped TiO_2 and TiO_2 nanostructured hybrids for enhanced photocatalysis, International journal of hydrogen energy. 45(13): pp. 7764-7778, 2020.

25. Kim, C.-S., J.-W. Shin, Y.-H. Cho, H.-D. Jang, H.-S. Byun, and T.-O. Kim, Synthesis and characterization of Cu/N-doped mesoporous TiO_2 visible light photocatalysts, Applied Catalysis A: General. 455: pp. 211-218, 2013.

26. Kim, T.-H., V. Rodríguez-González, G. Gyawali, S.-H. Cho, T. Sekino, and S.-W. Lee, Synthesis of solar light responsive Fe, N co-doped TiO_2 photocatalyst by sonochemical method, Catalysis today. 212: pp. 75-80, 2013.

27. Sun, M., H. Liu, Z. Sun, and W. Li, Donor-acceptor codoping effects on tuned visible light response of TiO_2, Journal of Environmental Chemical Engineering. 8(5): pp. 104168, 2020.

28. Devi, L.G. and R. Kavitha, A review on non metal ion doped titania for the photocatalytic degradation of organic pollutants under UV/solar light: Role of photogenerated charge carrier dynamics in enhancing the activity, Applied Catalysis B: Environmental. 140: pp. 559-587, 2013.

29. Nur, A.S., M. Sultana, A. Mondal, S. Islam, F.N. Robel, A. Islam, and M.S.A. Sumi, A review on the development of elemental and codoped TiO_2 photocatalysts for enhanced dye degradation under UV–vis irradiation, Journal of Water Process Engineering. 47: pp. 102728, 2022.

30. Xu, J., M. Sun, C. Zhang, M. Wu, and D. Fu, Electrochemical mineralization of Direct Blue 71 with boron-doped diamond anodes: Factor analysis and mechanisms study, Journal of Environmental Chemical Engineering. 10(1): pp. 107031, 2022.

31. Kumar, A., U. Dixit, K. Singh, S.P. Gupta, and M.S.J. Beg, *Structure and properties of dyes and pigments*, in *Dyes and pigments-novel applications and waste treatment*. 2021, IntechOpen.

32. Mani, S. and R.N. Bharagava, *Textile industry wastewater: Environmental and health hazards and treatment approaches*, in *Recent advances in environmental management*. 2018, CRC Press. p. 47-69.

33. Chequer, F.M.D., G.A.R. de Oliveira, E.R.A. Ferraz, J.C. Cardoso, M.V.B. Zanoni, and D.P. de Oliveira, *Textile dyes: Dyeing process and environmental impact*, in *Eco-friendly textile dyeing and finishing*. 2013, IntechOpen.

34. Etana, R., K. Angassa, and T. Getu, Dye removal from textile wastewater using scoria-based of vertical subsurface flow constructed wetland system, Scientific Reports. 15(1): pp. 949, 2025.

35. Leal Filho, W., P. Perry, H. Heim, M.A.P. Dinis, H. Moda, E. Ebhuoma, and A. Paço, An overview of the contribution of the textiles sector to climate change, Frontiers in environmental science. 10: pp. 973102, 2022.

36. Ghaly, A., R. Ananthashankar, M. Alhattab, and V.V. Ramakrishnan, Production, characterization and treatment of textile effluents: A critical review, J Chem Eng Process Technol. 5(1): pp. 1-19, 2014.

37. Yaseen, D. and M. Scholz, Textile dye wastewater characteristics and constituents of synthetic effluents: A critical review, International journal of environmental science and technology. 16: pp. 1193-1226, 2019.

38. Zahrim, A., C. Tizaoui, and N. Hilal, Evaluation of several commercial synthetic polymers as flocculant aids for removal of highly concentrated CI Acid Black 210 dye, Journal of hazardous materials. 182(1-3): pp. 624-630, 2010.

39. Anastopoulos, I., A. Hosseini-Bandegharaei, J. Fu, A.C. Mitropoulos, and G.Z. Kyzas, Use of nanoparticles for dye adsorption, Journal of Dispersion Science and Technology. 39(6): pp. 836-847, 2018.

40. Wang, X., C. Jiang, B. Hou, Y. Wang, C. Hao, and J. Wu, Carbon composite lignin-based adsorbents for the adsorption of dyes, Chemosphere. 206: pp. 587-596, 2018.

41. Harja, M., G. Buema, and D. Bucur, Recent advances in removal of Congo Red dye by adsorption using an industrial waste, Scientific Reports. 12(1): pp. 6087, 2022.

42. Nawaz, A., A. Farhan, F. Maqbool, H. Ahmad, W. Qayyum, E. Ghazy, A. Rahdar, A.M. Díez-Pascual, and S. Fathi-karkan, Zinc oxide nanoparticles: Pathways to micropollutant adsorption, dye removal, and antibacterial actions-A study of mechanisms, challenges, and future prospects, Journal of Molecular Structure. pp. 138545, 2024.

43. Dotto, J., M.R. Fagundes-Klen, M.T. Veit, S.M. Palácio, and R. Bergamasco, Performance of different coagulants in the coagulation/flocculation process of textile wastewater, Journal of cleaner production. 208: pp. 656-665, 2019.

44. Mcyotto, F., Q. Wei, D.K. Macharia, M. Huang, C. Shen, and C.W. Chow, Effect of dye structure on color removal efficiency by coagulation, Chemical Engineering Journal. 405: pp. 126674, 2021.

45. Ihaddaden, S., D. Aberkane, A. Boukerroui, and D. Robert, Removal of methylene blue (basic dye) by coagulation-flocculation with biomaterials (bentonite and *Opuntia ficus indica*), Journal of water process engineering. 49: pp. 102952, 2022.

46. Dadvar, E., R.R. Kalantary, H. Ahmad Panahi, and M. Peyravi, Efficiency of polymeric membrane graphene oxide-TiO_2 for removal of azo dye, Journal of Chemistry. 2017(1): pp. 6217987, 2017.

47. Gorgieva, S., R. Vogrinčič, and V. Kokol, The effect of membrane structure prepared from carboxymethyl cellulose and cellulose nanofibrils for cationic dye removal, Journal of Polymers and the Environment. 27: pp. 318-332, 2019.

48. Zhao, J., H. Liu, P. Xue, S. Tian, S. Sun, and X. Lv, Highly-efficient PVDF adsorptive membrane filtration based on chitosan@CNTs-COOH simultaneous removal of anionic and cationic dyes, Carbohydrate Polymers. 274: pp. 118664, 2021.

49. Coria-Oriundo, L.L., F. Battaglini, and S.A. Wirth, Efficient decolorization of recalcitrant dyes at neutral/alkaline pH by a new bacterial laccase-mediator system, Ecotoxicology and Environmental Safety. 217: pp. 112237, 2021.

50. Ali, S.S., J. Sun, E. Koutra, N. El-Zawawy, T. Elsamahy, and M. El-Shetehy, Construction of a novel cold-adapted oleaginous yeast consortium valued for textile azo dye wastewater processing and biorefinery, Fuel. 285: pp. 119050, 2021.

51. Ali, S.S., R. Al-Tohamy, and J. Sun, Performance of *Meyerozyma caribbica* as a novel manganese peroxidase-producing yeast inhabiting wood-feeding termite gut symbionts for azo dye decolorization and detoxification, Science of The Total Environment. 806: pp. 150665, 2022.

52. Azeez, F., E. Al-Hetlani, M. Arafa, Y. Abdelmonem, A.A. Nazeer, M.O. Amin, and M. Madkour, The effect of surface charge on photocatalytic degradation of methylene blue dye using chargeable titania nanoparticles, Scientific reports. 8(1): pp. 1-9, 2018.

53. Keerthana, S., R. Yuvakkumar, P.S. Kumar, G. Ravi, D.-V.N. Vo, and D. Velauthapillai, Influence of tin (Sn) doping on Co_3O_4 for enhanced photocatalytic dye degradation, Chemosphere. 277: pp. 130325, 2021.

54. Ohtani, B., Revisiting the fundamental physical chemistry in heterogeneous photocatalysis: its thermodynamics and kinetics, Physical chemistry chemical physics. 16(5): pp. 1788-1797, 2014.

55. Saravanan, R., F. Gracia, and A. Stephen, Basic principles, mechanism, and challenges of photocatalysis, Nanocomposites for visible light-induced photocatalysis. pp. 19-40, 2017.

56. Hassaan, M.A., M.A. El-Nemr, M.R. Elkatory, S. Ragab, V.-C. Niculescu, and A. El Nemr, Principles of photocatalysts and their different applications: A review, Topics in Current Chemistry. 381(6): pp. 31, 2023.

57. Rakshit Ameta, M.S.S., Surbhi Benjamin, Suresh C. Ameta, *Photocatalysis*, in *Advanced oxidation processes for wastewater treatment: emerging green chemical technology*, R.A. Suresh C. Ameta, Editor. 2018, Elsevier Inc. p. 135-175.

58. Khan, M.M., *Principles and mechanisms of photocatalysis*, in *Photocatalytic systems by design*. 2021, Elsevier. p. 1-22.

59. Wen, J., J. Xie, X. Chen, and X. Li, A review on g-C_3N_4-based photocatalysts, Applied surface science. 391: pp. 72-123, 2017.

60. Murugadoss, G., D.D. Kumar, M.R. Kumar, N. Venkatesh, and P. Sakthivel, Silver decorated CeO_2 nanoparticles for rapid photocatalytic degradation of textile rose bengal dye, Scientific Reports. 11(1): pp. 1080, 2021.

61. Ebrahimi, R., A. Maleki, Y. Zandsalimi, R. Ghanbari, B. Shahmoradi, R. Rezaee, M. Safari, S.W. Joo, H. Daraei, and S.H. Puttaiah, Photocatalytic degradation of organic dyes using WO_3-doped ZnO nanoparticles fixed on a glass surface in aqueous solution, Journal of Industrial and Engineering Chemistry. 73: pp. 297-305, 2019.

62. Khaokhajorn, C., P. Amornpitoksuk, C. Randorn, T. Rattana, and S. Suwanboon, One-pot synthesis of In_2O_3/ZnO nanocomposite photocatalysts and their enhanced photocatalytic activity against cationic and anionic dye pollutants, Inorganic Chemistry Communications. 157: pp. 111392, 2023.

63. Nagajyothi, P.C., S.V. Prabhakar Vattikuti, K.C. Devarayapalli, K. Yoo, J. Shim, and T.V.M. Sreekanth, Green synthesis: photocatalytic degradation of textile dyes using metal and metal oxide nanoparticles-latest trends and advancements, Critical Reviews in Environmental Science and Technology. 50(24): pp. 2617-2723, 2020.

64. Wu, H., Y. Li, and Q. Li, Facile synthesis of CuS nanostructured flowers and their visible light photocatalytic properties, Applied Physics A. 123: pp. 1-11, 2017.

65. Tsaviv, J., I. Eneji, R. Shato'Ato, I. Ahemen, P. Jubu, and Y. Yusof, Photodegradation, kinetics and non-linear error functions of methylene blue dye using $SrZrO_3$ perovskite photocatalyst, Heliyon. 10(14), 2024.

66. Wang, H., H. Wang, Z. Wang, L. Tang, G. Zeng, P. Xu, M. Chen, T. Xiong, C. Zhou, and X. Li, Covalent organic framework photocatalysts: structures and applications, Chemical Society Reviews. 49(12): pp. 4135-4165, 2020.

67. Khan, F., M.S. Khan, S. Kamal, M. Arshad, S.I. Ahmad, and S.A. Nami, Recent advances in graphene oxide and reduced graphene oxide based nanocomposites for the photodegradation of dyes, Journal of Materials Chemistry C. 8(45): pp. 15940-15955, 2020.

68. Guo, R.-t., J. Wang, Z.-x. Bi, X. Chen, X. Hu, and W.-g. Pan, Recent advances and perspectives of g–C_3N_4–based materials for photocatalytic dyes degradation, Chemosphere. 295: pp. 133834, 2022.

69. Saleh, S.M., ZnO nanospheres based simple hydrothermal route for photocatalytic degradation of azo dye, Spectrochimica Acta Part A: Molecular and Biomolecular Spectroscopy. 211: pp. 141-147, 2019.

70. Saini, D., R. Aggarwal, A.K. Sonker, and S.K. Sonkar, Photodegradation of azo dyes in sunlight promoted by nitrogen–sulfur–phosphorus codoped carbon dots, ACS Applied Nano Materials. 4(9): pp. 9303-9312, 2021.

71. Zhang, J., P. Zhou, J. Liu, and J. Yu, New understanding of the difference of photocatalytic activity among anatase, rutile and brookite TiO_2, Physical Chemistry Chemical Physics. 16(38): pp. 20382-20386, 2014.

72. Luttrell, T., S. Halpegamage, J. Tao, A. Kramer, E. Sutter, and M. Batzill, Why is anatase a better photocatalyst than rutile?-Model studies on epitaxial TiO_2 films, Scientific reports. 4(1): pp. 4043, 2014.

73. Ambrus, Z., K. Mogyorósi, Á. Szalai, T. Alapi, A. Dombi, and P. Sipos, Low temperature synthesis, characterization and substrate-dependent photocatalytic activity of nanocrystalline TiO_2 with tailor-made rutile to anatase ratio, Applied Catalysis A: General. 340(2): pp. 153-161, 2008.

74. Haggerty, J.E., L.T. Schelhas, D.A. Kitchaev, J.S. Mangum, L.M. Garten, W. Sun, K.H. Stone, J.D. Perkins, M.F. Toney, and G. Ceder, High-fraction brookite films from amorphous precursors, Scientific reports. 7(1): pp. 15232, 2017.

75. Žerjav, G., K. Žižek, J. Zavašnik, and A. Pintar, Brookite vs. rutile vs. anatase: Whats behind their various photocatalytic activities?, Journal of environmental chemical engineering. 10(3): pp. 107722, 2022.

76. Hanaor, D.A. and C.C. Sorrell, Review of the anatase to rutile phase transformation, Journal of Materials science. 46: pp. 855-874, 2011.

77. Li, H., X. Shen, Y. Liu, L. Wang, J. Lei, and J. Zhang, Facile phase control for hydrothermal synthesis of anatase-rutile TiO_2 with enhanced photocatalytic activity, Journal of Alloys and Compounds. 646: pp. 380-386, 2015.

78. Irfan, F., M.U. Tanveer, M.A. Moiz, S.W. Husain, and M. Ramzan, TiO_2 as an effective photocatalyst mechanisms, applications, and dopants: a review, The European Physical Journal B. 95(11): pp. 184, 2022.

79. Maleki, A., S. Nasseri, M. Hadi, and M. Solaimany Aminabad, Discoloration of aqueous Direct Blue 71 solutions using UV/H_2O_2/Nano-SiO_2 process, International Journal of Environmental Research. 9(2), 2015.

80. Makuła, P., M. Pacia, and W. Macyk, *How to correctly determine the band gap energy of modified semiconductor photocatalysts based on UV–Vis spectra*. 2018, ACS Publications. p. 6814-6817.

81. Wong, V.K., C. Zhang, Z. Zhang, M. Hao, Y. Zhou, and S.K. So, 0.01–0.5 sun is a realistic and alternative irradiance window to analyze urban outdoor photovoltaic cells, Materials Today Energy. 36: pp. 101347, 2023.

82. Schneider, J.T., D.S. Firak, R.R. Ribeiro, and P. Peralta-Zamora, Use of scavenger agents in heterogeneous photocatalysis: truths, half-truths, and misinterpretations, Physical Chemistry Chemical Physics. 22(27): pp. 15723-15733, 2020.

83. Shah, J.H., M. Fiaz, M. Athar, J. Ali, M. Rubab, R. Mehmood, S.U.U. Jamil, and R. Djellabi, Facile synthesis of N/B-double-doped Mn_2O_3 and WO_3 nanoparticles for dye degradation under visible light, Environmental Technology. 2020.

84. Molaei, P. and F. Rahimi-Moghadam, Porous g-C_3N_4 nanosheets through facile thermal polymerization of melamine in the air for photocatalyst application, Journal of Materials Science: Materials in Electronics. 32: pp. 19655-19666, 2021.

85. Al-Qaradawi, S. and S.R. Salman, Photocatalytic degradation of methyl orange as a model compound, Journal of Photochemistry and photobiology A: Chemistry. 148(1-3): pp. 161-168, 2002.

86. Krýsa, J., M. Keppert, J.r. Jirkovský, V. Štengl, and J. Šubrt, The effect of thermal treatment on the properties of TiO_2 photocatalyst, Materials Chemistry and Physics. 86(2-3): pp. 333-339, 2004.

87. Ganesh, I., A. Gupta, P. Kumar, P. Sekhar, K. Radha, G. Padmanabham, and G. Sundararajan, Preparation and characterization of Ni-doped TiO_2 materials for photocurrent and photocatalytic applications, The Scientific World Journal. 2012(1): pp. 127326, 2012.

88. Aware, D.V. and S.S. Jadhav, Synthesis, characterization and photocatalytic applications of Zn-doped TiO_2 nanoparticles by sol–gel method, Applied Nanoscience. 6(7): pp. 965-972, 2016.

89. Reda, S., M. Khairy, and M. Mousa, Photocatalytic activity of nitrogen and copper doped TiO_2 nanoparticles prepared by microwave-assisted sol-gel process, Arabian Journal of Chemistry. 13(1): pp. 86-95, 2020.

90. Gomez-Polo, C., S. Larumbe, A. Gil, D. Muñoz, L.R. Fernández, L.F. Barquín, A. García-Prieto, M. Fdez-Gubieda, and A. Muela, Improved photocatalytic and antibacterial performance of Cr doped TiO_2 nanoparticles, Surfaces and Interfaces. 22: pp. 100867, 2021.

91. Villarreal-Morales, R., L. Hinojosa-Reyes, R. Zanella, J.C. Durán-Álvarez, A. Caballero-Quintero, and J.L. Guzmán-Mar, Enhanced performance of TiO_2 doped with aluminum for the photocatalytic degradation of a mixture of plasticizers, Journal of Environmental Chemical Engineering. 10(1): pp. 107100, 2022.

92. Rosa, D., N. Abbasova, and L. Di Palma, Titanium dioxide nanoparticles doped with iron for water treatment via photocatalysis: A review, Nanomaterials. 14(3): pp. 293, 2024.

93. Huang, F., A. Yan, and H. Zhao, Influences of doping on photocatalytic properties of TiO_2 photocatalyst, Semiconductor photocatalysis: materials, mechanisms and applications. pp. 31, 2016.

94. Irie, H., Y. Watanabe, and K. Hashimoto, Nitrogen-concentration dependence on photocatalytic activity of $TiO_{2-x}N_x$ powders, The Journal of Physical Chemistry B. 107(23): pp. 5483-5486, 2003.

95. Zhao, Q., Y. Ren, L. Huang, Y. Chen, and Z. Bian, In situ Fe (III)-doped TiO_2 mesocrystals catalyzed visible light photo-Fenton system, Catalysis Today. 410: pp. 309-316, 2023.

96. Kumar, K.A., K. Subalakshmi, and J. Senthilselvan, Effect of mixed valence state of titanium on reduced recombination for natural dye-sensitized solar cell applications, Journal of Solid State Electrochemistry. 20: pp. 1921-1932, 2016.

97. Khan, H. and I.K. Swati, Fe^{3+}-doped anatase TiO_2 with *d–d* transition, oxygen vacancies and Ti^{3+} centers: synthesis, characterization, UV–vis photocatalytic and mechanistic studies, Industrial & Engineering Chemistry Research. 55(23): pp. 6619-6633, 2016.

98. Abidov, A., B. Allabergenov, J. Lee, H.-W. Jeon, S.-W. Jeong, and S. Kim, X-ray photoelectron spectroscopy characterization of Fe doped TiO_2 photocatalyst, Int. J. Mater. Mech. Manuf. 1(3): pp. 294, 2013.

99. Reddy, Y.A.K., I.-K. Kang, Y.B. Shin, and H.C. Lee, Bolometric properties of reactively sputtered TiO_{2-x} films for thermal infrared image sensors, Journal of Physics D: Applied Physics. 48(35): pp. 355104, 2015.

100. Duan, Z., A. Zhong, Q. Tang, H. Wang, and Z. Wu, Oxygen vacancies induce boosted photocarriers dynamics in WO3/Ti_3C_2 micro-nano structures with enriched 2D-2D interfaces for trimethylamine abatement, Chemical Engineering Journal. 2025.

101. Miao, Z., G. Wang, X. Zhang, and X. Dong, Oxygen vacancies modified TiO_2/Ti_3C_2 derived from MXenes for enhanced photocatalytic degradation of organic pollutants: The crucial role of oxygen vacancy to Schottky junction, Applied Surface Science. 528: pp. 146929, 2020.

102. Kumar, A., P. Raizada, A.A.P. Khan, V.-H. Nguyen, Q. Van Le, A. Singh, V. Saini, R. Selvasembian, T.-T. Huynh, and P. Singh, Phenolic compounds degradation: Insight into the role and evidence of oxygen vacancy defects engineering on nanomaterials, Science of the Total Environment. 800: pp. 149410, 2021.

103. Ajmal, A., I. Majeed, R.N. Malik, H. Idriss, and M.A. Nadeem, Principles and mechanisms of photocatalytic dye degradation on TiO_2 based photocatalysts: a comparative overview, Rsc Advances. 4(70): pp. 37003-37026, 2014.

104. Nosaka, Y. and A. Nosaka, Understanding hydroxyl radical (•OH) generation processes in photocatalysis, ACS Energy Letters. 1(2): pp. 356-359, 2016.